

## Timing and dynamics of glaciation in the Ikh Turgen Mountains, Altai region, High Asia



Robin Blomdin<sup>a,b,\*</sup>, Arjen P. Stroeven<sup>a,b</sup>, Jonathan M. Harbor<sup>a,b,c</sup>, Natacha Gribenski<sup>a,b,d</sup>, Marc W. Caffee<sup>c,e</sup>, Jakob Heyman<sup>f</sup>, Irina Rogozhina<sup>g</sup>, Mikhail N. Ivanov<sup>h</sup>, Dmitry A. Petrakov<sup>h</sup>, Michael Walther<sup>i</sup>, Alexei N. Rudoy<sup>j</sup>, Wei Zhang<sup>k</sup>, Alexander Orkhonselenge<sup>l</sup>, Clas Hättestrand<sup>a,b</sup>, Nathaniel A. Lifton<sup>c,e</sup>, Krister N. Jansson<sup>a,b</sup>

<sup>a</sup> Geomorphology and Glaciology, Department of Physical Geography, Stockholm University, Stockholm, Sweden

<sup>b</sup> Bolin Centre for Climate Research, Stockholm University, Stockholm, Sweden

<sup>c</sup> Department of Earth, Atmospheric, and Planetary Sciences, Purdue University, West Lafayette, USA

<sup>d</sup> Institute of Geological Sciences, University of Bern, Bern, Switzerland

<sup>e</sup> Department of Physics and Astronomy, Purdue University, West Lafayette, USA

<sup>f</sup> Department of Earth Sciences, University of Gothenburg, Gothenburg, Sweden

<sup>g</sup> MARUM, University of Bremen, Bremen, Germany

<sup>h</sup> Faculty of Geography, Lomonosov Moscow State University, Moscow, Russia

<sup>i</sup> Institute of Geography and Geoecology, Mongolian Academy of Sciences, Ulaanbaatar, Mongolia

<sup>j</sup> Center of Excellence for Biota, Climate and Research, Tomsk State University, Tomsk, Russia

<sup>k</sup> College of Urban and Environmental Science, Liaoning Normal University, Dalian, China

<sup>l</sup> Laboratory of Geochemistry and Geomorphology, School of Arts and Sciences, National University of Mongolia, Ulaanbaatar, Mongolia

### ARTICLE INFO

#### Keywords:

Altai  
Ikh Turgen mountains  
Chikhacheva range  
Paleoglaciology  
Glacial geomorphology  
<sup>10</sup>Be surface exposure dating  
Geomorphometric analysis

### ABSTRACT

Spanning the northern sector of High Asia, the Altai region contains a rich landform record of glaciation. We report the extent, chronologies, and dynamics of two paleoglaciers on opposite flanks of the Ikh Turgen mountains (In Russian: Chikhacheva Range), straddling the border between Russia and Mongolia, using a combination of remote sensing-based glacial geomorphological mapping, <sup>10</sup>Be surface exposure dating, and geomorphometric analysis. On the eastern side (Mongolia), the Turgen-Asgt paleoglacier, with its potential for developing a large accumulation area (~257 km<sup>2</sup>), expanded 40 km down valley, and mean ages from a latero-frontal moraine indicate deglaciation during marine oxygen isotope stage (MIS) 3 (45.1 ± 1.8 ka, n = 4) and MIS 2 (22.8 ± 3.3 ka, n = 5). These minimum age constraints are consistent with other <sup>10</sup>Be glacial chronologies and paleoclimate records from the region, which indicates glacier culmination during cold and wet conditions coinciding with MIS 3 ( piedmont-style glaciation; inferred for a few sites across the region) and glacier culmination during cold and dry conditions coinciding with MIS 2 (mainly valley-style glaciation; inferred from several sites across the region). On the western side (Russia), the Boguty paleoglacier had a smaller accumulation area (~222 km<sup>2</sup>), and advanced 30 km down valley across a low gradient forefield. Surface exposure ages from two moraine complexes on this side of the mountains exhibit wide scatter (~14–53 ka, n = 8), making paleoclimate inferences and comparison to other proxies difficult. Ice surface profile reconstructions imply that the two paleoglaciers likely shared an ice divide.

### 1. Introduction

The Altai Mountains are located in the northern sector of High Asia (Fig. 1); a rugged and land-locked region consisting of a series of NW–SE trending mountain ranges, with maximum elevations of up to ~4500 m a.s.l. High Asia is located at the convergence of several atmospheric circulation systems. In the Altai Mountains, during summers,

the Mid-Latitude Westerlies (MLW) deliver humid air masses from the Atlantic Ocean. During winters, the Siberian High-pressure system (SH) brings cold and dry air masses from the Arctic, deflecting the Mid-Latitude Westerlies further to the south (Cheng et al., 2012, Fig. 1 inset map). Migration of these air circulation systems causes large annual and seasonal differences in precipitation partitioning and temperature (Gillespie and Molnar, 1995; Rupper and Roe, 2008). Other large

\* Corresponding author. Geomorphology and Glaciology, Department of Physical Geography, Stockholm University, Stockholm, Sweden.  
E-mail address: [robin.blomdin@natgeo.su.se](mailto:robin.blomdin@natgeo.su.se) (R. Blomdin).

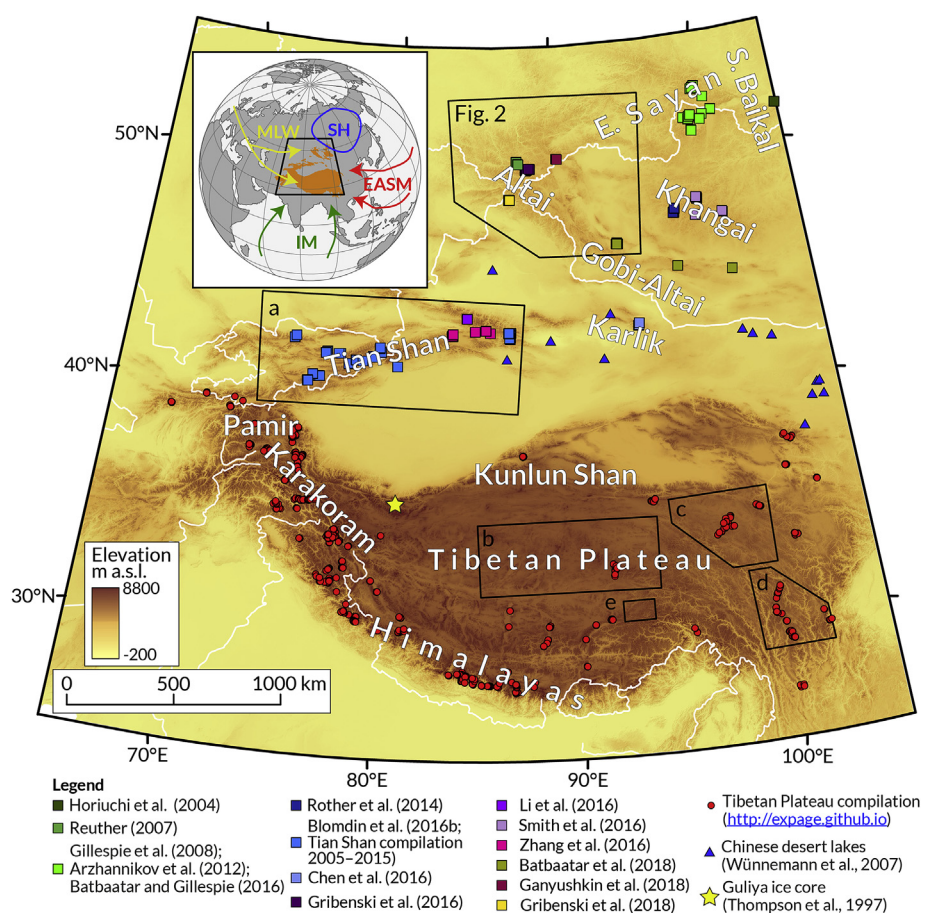


**Fig. 1.** Physiography of High Asia. Locations of previously mapped regions indicated with black boxes (cf. Fig. 2 for the Altai and western Sayan mountains; Blomdin et al., 2016a); a) the Tian Shan (Stroeven et al., 2013), b) the central Tibetan Plateau (Morén et al., 2011), c) Bayan Har Shan (Heyman et al., 2008), d) Shaluli Shan (Fu et al., 2012), and e) the Maidika region (Lindholm and Heyman, 2015). Also indicated are the locations of all published  $^{10}\text{Be}$  surface exposure age samples ( $n = 2699$ ) from glacial settings across High Asia (extracted from: <http://expage.github.io>), the location of the Guliya ice core (Thompson et al., 1997) and Chinese desert lake core records (Wünnemann et al., 2007). References are provided for studies mentioned in the text and illustrated in Figs. 9 and 10. Inset map shows the location of High Asia, with topography higher than 2000 m a.s.l. shaded orange and locations of major atmospheric circulation systems, SH = Siberian High-pressure system, MLW = Mid-Latitude Westerlies, IM = Indian Monsoon and EASM = East Asian Summer Monsoon (Cheng et al., 2012). (For interpretation of the references to colour in this figure legend, the reader is referred to the Web version of this article.)

atmospheric circulation systems prevailing across High Asia are the Indian and East Asian summer monsoons (IM & EASM), but these have little or no effect on the Altai Mountains today (Winkler and Wang, 1993, Fig. 1 inset map). In addition to the interaction between the Siberian High and the Mid-Latitude Westerlies, the pronounced topography of the Altai Mountains also produces steep precipitation gradients from west to east (Tronov, 1949; Dolgushin and Osipova, 1989; Klinge et al., 2003; Lehmkuhl et al., 2004), depleting the westerly sourced moisture and causing rain shadow effects on the eastern flanks of Altai Mountains.

Glaciers located at the confluence of major circulation systems are particularly sensitive to their climate variability (Rupper and Roe, 2008; Rupper et al., 2009). Hence, the topographic and climatic settings of the Altai Mountains impact the evolution and distribution of glaciers, both present-day and Pleistocene glaciers (Lehmkuhl et al., 2016). In general, present-day glaciers occur at lower altitudes in the wetter northwestern regions of the Altai rather than in the drier eastern regions (Lehmkuhl et al., 2004; 2011; 2016; Nuimura et al., 2015). The spatial pattern of present-day glacier area change varies significantly across the different sectors of the Altai Mountains; glaciers in the Chuya and Kurai basins (Fig. 2), in the Russian Altai, exhibited glacier area change of  $-9\text{--}27\%$  between the years 1952 and 2008 (Narozhniy and Zemtsov, 2011), while glacier area changes in the Mongolian Altai varied between  $+10$  to  $-36\%$  for the years 1990 and 2010 (Kamp and Pan, 2015). This spatial variation in modern glacier area change likely both reflect regional climate change (generally warming trend) and differences in glacier morphologies (Kamp and Pan, 2015).

Understanding the timing and dynamics of past glaciation in the Altai Mountains provides insight into how glaciers across a mountain system respond to regional climate change. Reconstructed paleoglacier extents can be used as paleoclimate proxies; glacier expansion and

retreat of a glacier is a function of variations in air temperature and precipitation (e.g. Oerlemans et al., 1998). Topographic factors may also control the extent and dynamics of glaciation. Large, high-elevation catchments, for example, are more likely to sustain large glaciers compared to small low-elevation catchments. Catchment morphology, valley width, length, slope and aspect, also influence glacier dynamics (Barr and Lovell, 2014). While topographic factors affect the style of glaciation, chronologies reconstructed from glacial deposits across a large area may provide location-specific nodes of local climate information (Kirkbride and Winkler, 2012). If glaciers spanning a large region behave similarly (i.e. synchronous expanding or retreat), the glaciers are likely responding to regional-scale climate variations as opposed to local non-climatic factors (Rupper and Roe, 2008).

Proposed glacial reconstructions for the Altai region, range from limited alpine style-glaciation with centres of glaciation consisting of ice caps and ice fields (Lehmkuhl et al., 2004; Lehmkuhl and Owen, 2005; Blomdin et al., 2016a) to a large ice sheet covering the Altai Mountains (Grosswald et al., 1994; Grosswald and Rudoy, 1996; Rudoy, 2002). Although most studies support limited alpine style-glaciation, additional mapping, dating, and modelling studies will provide quantitative constraints on the timing and dynamics of glaciation. The extent of past glaciation in the Altai Mountains can be evaluated using extensive marginal moraine deposits, located beyond the main mountain fronts (Blomdin et al., 2016a). These glacial deposits indicate a style of Pleistocene glaciation comprised of valley glaciers, as well as ice caps and ice fields, in which large outlet glaciers extended well beyond the mountain fronts onto the lowlands or intermontane basins (Lehmkuhl et al., 2004; 2016; Blomdin et al., 2016a). The dynamics and style of Pleistocene glacier cover has been extensively characterized (cf. Grosswald et al., 1994; Grosswald and Rudoy, 1996; Lehmkuhl, 1998; 2012; Lehmkuhl et al., 2004; 2011; 2016; Blomdin et al., 2016a). Fewer

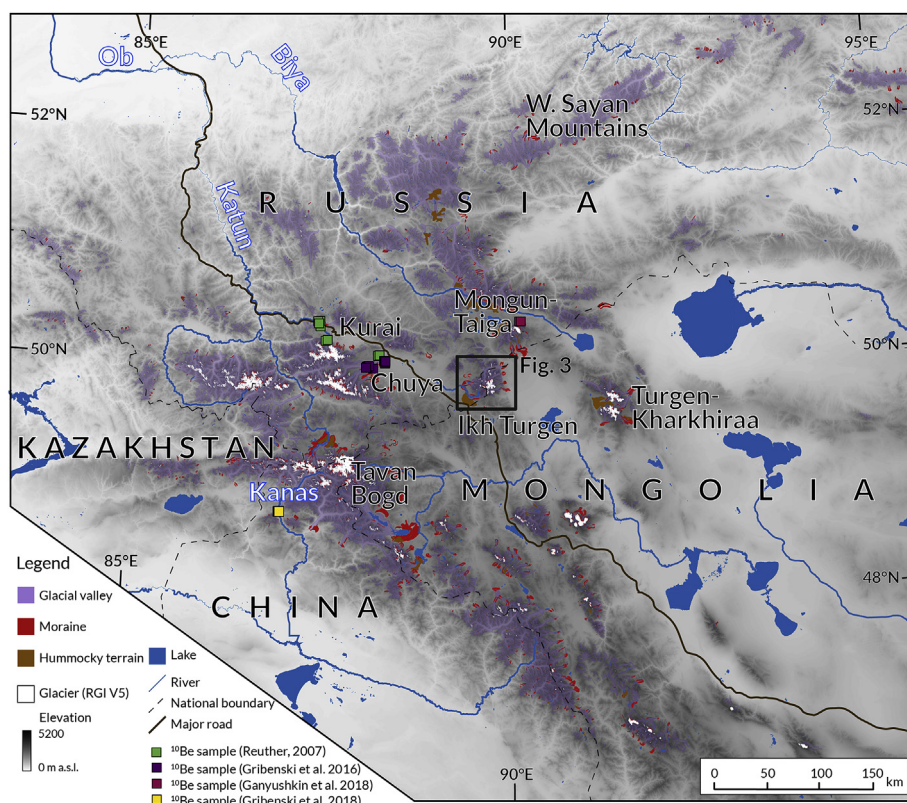


**Fig. 2.** Physiography and glacial geomorphology of the Altai and western Sayan mountains (Blomdin et al., 2016a), the distribution of present-day glaciers (Arendt et al., 2015; Niumura et al., 2015; Randolph Glacier Inventory [RGI] V5), and locations of published  $^{10}\text{Be}$  surface exposure age samples from glacial deposits.

studies focus on the timing of glaciation using geochronological techniques such as optically stimulated luminescence (OSL) dating and *in situ* cosmogenic nuclide (e.g.  $^{10}\text{Be}$  or  $^{26}\text{Al}$ ) surface exposure dating. Recent studies in the Chuya and Kurai basins (Reuther et al., 2006; Reuther, 2007; Gribenski et al., 2016), the Kanas Valley (Zhao et al., 2013; Gribenski et al., 2018), the Mongun-Taiga massif (Ganyushkin et al., 2018) and the Tavan Bogd catchment (Lehmkuhl et al., 2016) (Fig. 2) indicate glacier culmination in the Altai Mountains during marine oxygen-isotope stage (MIS) 2 (14–29 ka), MIS 3 (29–57 ka), MIS 4 (57–71 ka) and MIS 6 (130–191 ka).

Glacial chronologies are also available from ranges in the vicinity of the Altai: the Tian Shan (Hubert-Ferrari et al., 2005; Koppes et al., 2008; Kong et al., 2009; Li et al., 2011, 2016; 2014; Zech, 2012; Lifton et al., 2014a; Blomdin et al., 2016b; Zhang et al., 2016), the Karlik Range (Chen et al., 2015); the Khangai Mountains (Rother et al., 2014; Smith et al., 2016; Batbaatar et al., 2018); the Eastern Sayan Mountains (Gillespie et al., 2008; Arzhannikov et al., 2012; Batbaatar and Gillespie, 2016), the Gobi-Altai ranges (Batbaatar et al., 2018); and the southern part of the Baikal region (Horiuchi et al., 2004) (Fig. 1). These studies provide a broader context for our own investigations. Many glaciers across High Asia seem to have reached their maximum positions before the global last glacial maximum (LGM; 19–26.5 ka) which broadly falls within MIS 2 (Clark et al., 2009; Hughes et al., 2013). This is supported by a small but growing dataset of glacial chronologies indicating that maximum glacier culmination occurred during MIS 3 and MIS 5 (e.g. Li et al., 2014; Rother et al., 2014; Blomdin et al., 2016b). Given the uncertainties of  $^{10}\text{Be}$  surface exposure and OSL dating, the timing of glacier culmination prior to MIS 2 are often difficult to constrain (e.g. Gribenski et al., 2018). A combination of sparse data (i.e. dated glacial deposits) and a large spread in the data have so far precluded correlation of regional-scale glacier culmination prior to MIS 2.

In this work we investigate the timing and dynamics of glaciation in

the Ikh Turgen mountains, a range in the central region of the Altai. The specific objectives are:

- 1) Mapping and identifying the maximum extent of past glaciation in the Ikh Turgen mountains, using remote sensing-based geomorphological mapping.
- 2) Establishing glacial chronologies for the Boguty and Turgen-Asgat catchments, using  $^{10}\text{Be}$  surface exposure dating of glacial deposits.
- 3) Reconstructing the ice surface profiles of the Boguty and Turgen-Asgat paleoglaciers, using geomorphometric analysis (analysis of digital elevation models in a Geographic Information System, GIS) and a simple 2-D ice profiling tool (Benn and Hulton, 2010).
- 4) Inferring past glacier dynamics of the Boguty and Turgen-Asgat paleoglaciers using a combination of data generated in objectives 1–3.
- 5) Comparing and contrasting the Ikh Turgen glacial chronology with other glacial chronologies and proxy records from the northern sector of High Asia, including the Tian Shan.

## 2. Background

### 2.1. Study area

The Altai Mountains are the northernmost far-field effects of the Cenozoic India-Asia collision (Molnar and Tapponnier, 1975). A series of right-slip faults, which alternate with extensive intermontane basins, extends, from the westernmost Tian Shan to the eastern border of the Altai Mountains (Yin, 2010, Fig. 1). Several large river systems drain the Altai Mountains. The Katun and Biya rivers drain the southern catchments and are tributaries of the Ob River, which flows from the Altai to the Arctic Ocean (Fig. 2). The rivers of the Mongolian sector drain towards large endorheic (internally drained) intermontane basins (Fig. 2). Lake Kanas and the Kanas River drains the southern Chinese

Altai Mountains and are also part of the southernmost catchment area of the Ob River (Fig. 2). The Ikh Turgen mountains (in Russian: Chikhacheva Range) are located on the border between Russia and Mongolia (Fig. 2). The range consists of three major catchments draining

towards the west and five draining towards the east; the Boguty and Turgen-Asgat catchments contain the largest and longest trunk valleys, and because of the geometry of the range, the only west–east opposing catchments sharing a water divide at their headwalls (Fig. 3).

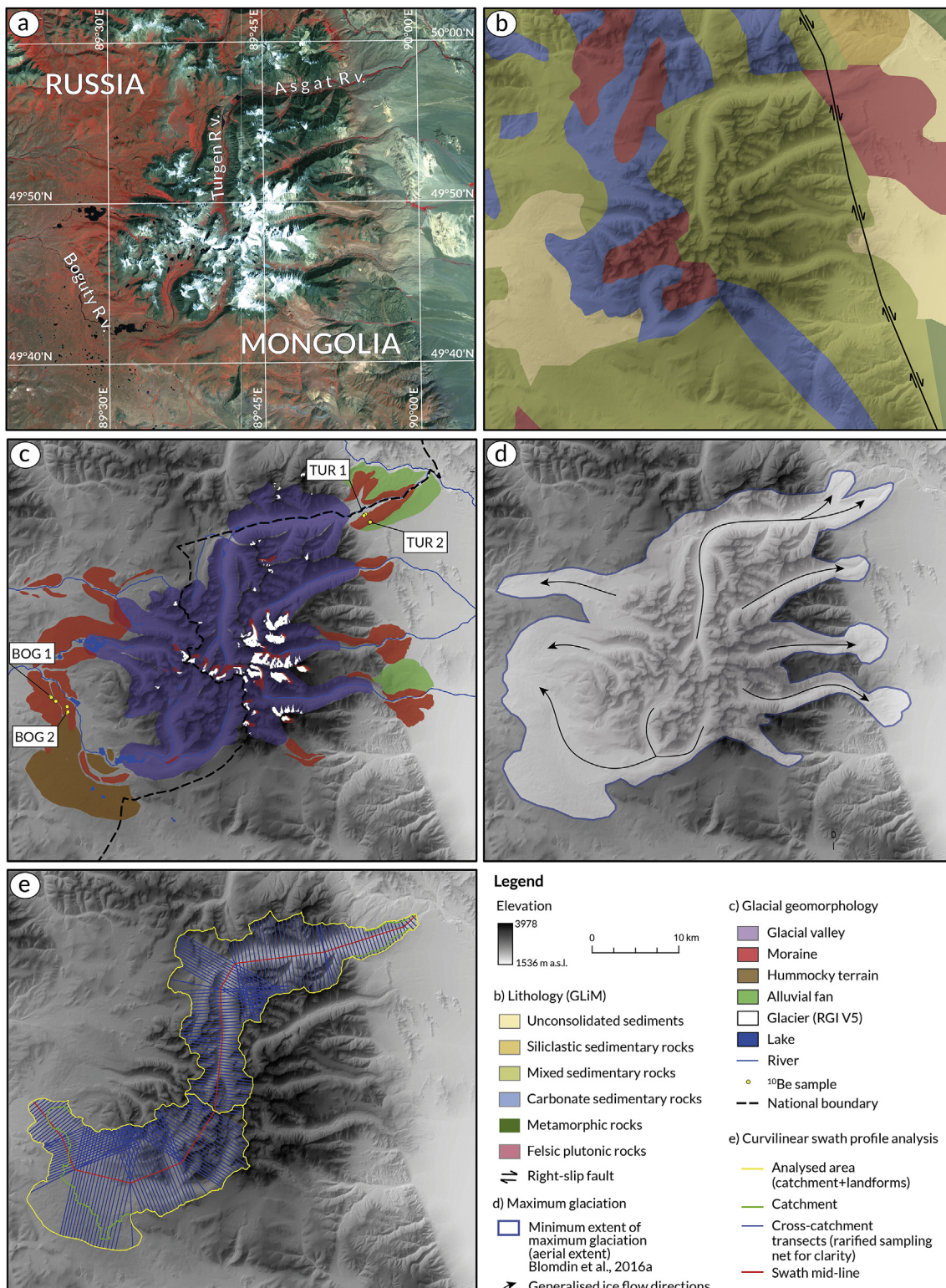


**Fig. 3.** Physiography of the Ikh Turgen mountains (In Russian: Chikhacheva Range). See Fig. 2 for location. a) Landsat 8 False-IR colour composite, b) lithology; general rock types (GLiM; Hartmann and Moosdorf, 2012), c) glacial geomorphology, alluvial fans (this study), present-day glaciers (Arendt et al., 2015; Nuimura et al., 2015; Randolph Glacier Inventory [RGI] V5), and <sup>10</sup>Be sample locations, d) minimum extent of maximum glaciation (aerial extent) and generalised ice flow directions (based on mapped landforms in Blomdin et al., 2016a), and e) illustration of the curvilinear swath profile reconstruction of the Boguty and Turgen-Asgat catchments (see Fig. 7). (For interpretation of the references to colour in this figure legend, the reader is referred to the Web version of this article.)

We have targeted the Boguty and Turgen-Asgat catchments for detailed paleoglaciological investigation because they display extensive glacial deposits, and they mark the water divide between the Ob River catchment and the eastern Altai Mountains. The Ikh Turgen mountains are also located along a west–east transect that includes previous paleoglaciological studies to the west in the Chuya and Kurai basins in Russia (Reuther et al., 2006; Reuther, 2007; Gribenski et al., 2016; Agatova and Nepop, 2017), to the northeast in the Mongun-Taiga massif (Ganyushkin et al., 2018) and to the east in the Turgen-Khar-khiraa Mountains in Mongolia (Lehmkuhl et al., 2004, Fig. 2). The Boguty and Turgen-Asgat catchments also display strikingly different characteristics. The upper part of the Boguty catchment contains felsic plutonic rocks (granites and their relatives) and carbonate sedimentary rocks (limestone, dolomite, or marl), while the lower part consists of unconsolidated sediment (Hartmann and Moosdorf, 2012, Fig. 3b). The Turgen-Asgat catchment consists mainly of mixed sedimentary rocks (including interlayered sandstone and limestone) along the trunk valley, while a local pluton of granitic rocks exists at the mountain front (Hartmann and Moosdorf, 2012, Fig. 3b). Delineating the eastern mountain front is a NNW striking right-slip fault, the Ar Höölg Fault (Cunningham, 2005, Fig. 3b).

In the lower parts of the Boguty catchment there is a flat foreland basin, draped by widespread glacial deposits, including hummocky terrain (Lehmkuhl et al., 2004; Blomdin et al., 2016a, Fig. 3c). In comparison, the lower parts of the Turgen-Asgat catchments are truncated by the Ar Höölg Fault, and extensive moraine deposits occur on top of large alluvial fans (Lehmkuhl et al., 2004, Fig. 3c). Only ~3 small glaciers currently exist in the Boguty catchment—with southerly or easterly aspects, while there are ~10 small glaciers in the upper tributaries of the Turgen-Asgat catchment—with northerly and westerly aspects (Fig. 3; Arendt et al., 2015; Nuimura et al., 2015; Randolph Glacier Inventory [RGI] V5). The differences in valley geometries between the western and eastern catchments also influenced former ice margin outlines—the western catchments are generally smaller and have a shorter distance between their headwalls and the mountain front, while the eastern catchments are larger and have longer distances between their headwalls and the mountain front. A minimum extent of maximum glaciation (aerial extent) reconstruction (Fig. 3d) indicates that on the western side of the mountains, paleoglaciers coalesced to form two separate ice lobes, while on the eastern side four main valley paleoglaciers drained the mountain (Lehmkuhl et al., 2004; Blomdin et al., 2016a). The western side of Ikh Turgen also constitutes the eastern part of the Chuya Basin; the Boguty River (Figs. 2 and 3c) drains west towards the Chuya and Kurai basins, which are tectonic intermontane basins. Paleoglaciers in these basins impounded extensive glacial lakes in the depressions, which later drained catastrophically via the Katun and Ob rivers at ~19 ka (cf. Rudoy and Baker, 1993; Reuther et al., 2006; Gribenski et al., 2016).

### 3. Methods

#### 3.1. Glacial geomorphological mapping

We mapped glacial landforms from remotely sensed data to investigate the extent and dynamics of glaciation in the Ikh Turgen mountains, using the methodology described in Heyman et al. (2008). The mapping is performed in a GIS environment using visual interpretation of Landsat 8 imagery, and the Shuttle Radar Topographic Mission (SRTM) Digital Elevation Model (DEM) 30. The SRTM 30 has a one-arc second resolution, which is about  $30 \times 30$  m per pixel, and the resolution of the Landsat imagery is also  $30 \times 30$  m (panchromatic band:  $15 \times 15$  m). Both datasets were accessed from the USGS web portal Earth Explorer (<https://earthexplorer.usgs.gov/>). The mapping work herein extends the map by Blomdin et al. (2016a) by examining

Landsat 8 imagery and mapping individual moraine ridges and alluvial fans (Fig. 3c). Fieldwork performed in 2013 and 2014 validated our mapping. Based on this new landform map we delineate the minimum extent of maximum glaciation by tracing the outer limits of the glacial landforms (cf. Blomdin et al., 2016a). The new mapping and maximum glaciation reconstruction is available in the supplementary data as ESRI ArcGIS shapefiles.

#### 3.2. *In situ* $^{10}\text{Be}$ surface exposure dating

To determine the timing of deglaciation in the Ikh Turgen mountains we obtained exposure ages using cosmogenic  $^{10}\text{Be}$  (cf. Gosse and Phillips, 2001; Phillips et al., 2016). We sampled quartz-rich granitic boulders on moraine crests or on the flat upper surfaces of latero-frontal moraines. All boulder samples were processed at PRIME Lab, Purdue University. Quartz was separated from the whole rock using standard mineral separation techniques. The purity of the quartz was verified by ICP-OES measurements. The purified quartz samples (Al-concentrations < 200 ppm) were dissolved after being spiked with a Be carrier ( $^9\text{Be}$  concentration:  $1069 \pm 8$  ppm) and Be was isolated using chromatographic techniques (Kohl and Nishiizumi, 1992) and loaded into targets as BeO for accelerator mass spectrometry (AMS) measurement. The  $^{10}\text{Be}/^9\text{Be}$  ratios were measured at PRIME Lab (Sharma et al., 2000). Ratios were obtained through normalization with a standard having a  $^{10}\text{Be}/^9\text{Be}$  ratio of  $2.85 \pm 10^{-12}$  (Nishiizumi et al., 2007). Beryllium-10 concentrations are obtained from the ratio, the amount of sample dissolved, and the amount of  $^9\text{Be}$  carrier added to the sample. The  $^{10}\text{Be}$  concentration uncertainties reflect measurement uncertainty, blank subtraction, and uncertainty in the concentration and amount of Be added as carrier. Table 1 contains the  $^{10}\text{Be}$  sample information.

We calculated surface exposure ages by using the modified CRONUS calculator (Balco et al., 2008) after Heyman et al. (2016; <http://expage.github.io/calculator/expage-201708.zip>). In the calculation, corrections for topographic shielding are included. We used a global reference spallation production rate of  $3.98 \pm 0.25$  atoms g $^{-1}$  year $^{-1}$  based on a global set of calibration sites (2009–2016; <http://expage.github.io>). Notable characteristics of the calculator are:

1. Spallation production rate scaling are based on the time-dependent and nuclide-specific LSDn scaling (Lifton et al., 2014b).
2. Muon production rate parameterization based on a modified version of the LSD scaling (Lifton et al., 2014b) and the CRONUScalc calculator (Marrero et al., 2016) with calculator specific calibration against the Beacon Height depth profile data (Balco, 2017).
3. Attenuation length for calculating the production rate adjustments for sample thickness and erosion rate interpolated from the atmospheric pressure and cut-off rigidity (Marrero et al., 2016).
4. Atmospheric pressure interpolation based on the ERA-40 re-analysis dataset (Uppala et al., 2005).

Errors of exposure ages are represented by the internal uncertainty (error in blank, carrier mass, counting statistics). When calculating ages of moraine surfaces (ridge crests, flat upper surface of latero-frontal moraines) we adopt the arithmetic mean ( $X_m$ ) and standard deviation ( $\sigma$ ) of boulder exposure ages as a representation of the age and uncertainty of deglaciation (Shakun et al., 2015; Blomdin et al., 2016b). We also include the reference production rate uncertainty added in quadrature (Shakun et al., 2015). Before assigning deglaciation ages of moraine surfaces, we test the boulder populations for outliers using Peirce's criterion (Peirce, 1852; 1877; Gould, 1855; Ross, 2003). A sample in a population is rejected if its deviation from the group average is larger than the maximum allowed deviation. This threshold is determined by multiplying the standard deviation of the sample with R (“the ratio of maximum allowable deviation from the data mean to

**Table 1**  $^{10}\text{Be}$  sample information.  $^{10}\text{Be}$  concentrations were calculated from  $^{10}\text{Be}/^{9}\text{Be}$  ratios measured by Accelerator Mass Spectrometry (AMS) at PRIME Lab, Purdue University in 2015 normalized to standards with a  $^{10}\text{Be}/^{9}\text{Be}$  ratio of  $2.85 \times 10^{-12}$  (Nishizumi et al., 2007) and using a  $^{10}\text{Be}$  half-life of  $1.387 \times 10^6$  years (Chmeleff et al., 2010; Korschinek et al., 2010). All samples were spiked with the PRIME Lab in-house  $^{9}\text{Be}$  carrier with a concentration of  $1.069 \pm 8$  ppm. Three different blanks were used for the background correction: For samples AL14-01 to AL14-05; blank carrier mass  $0.2684\text{ g}$ ,  $^{10}\text{Be}/^{9}\text{Be}$  ratio  $2.567 \pm 1.018 \times 10^{-15}$ . For samples AL13-C-015 to AL-13-C-020; blank carrier mass  $0.2695\text{ g}$ ,  $^{10}\text{Be}/^{9}\text{Be}$  ratio of  $6.829 \pm 1.427 \times 10^{-15}$ ,  $^{10}\text{Be}/^{9}\text{Be}$  ratio of  $6.829 \pm 1.427 \times 10^{-15}$ ,  $^{10}\text{Be}/^{9}\text{Be}$  ratio of  $6.829 \pm 1.427 \times 10^{-15}$ ,  $^{10}\text{Be}/^{9}\text{Be}$  ratio of  $6.829 \pm 1.427 \times 10^{-15}$ . All  $^{10}\text{Be}$  surface exposure ages are reported with zero surface erosion, hence results are minimum ages. Topographic shielding was established in the field measuring azimuth and horizon angles and computed with the geometric shielding calculator at: [https://hess.ess.washington.edu/math/general/skyline\\_input.php](https://hess.ess.washington.edu/math/general/skyline_input.php). Rock density correction applied is  $2.65\text{ g cm}^{-3}$ . Ages are reported using the nuclide-specific LSD production rate scaling (Lifton et al., 2014) and an updated global reference production rate of  $3.98 \pm 0.25\text{ atoms g}^{-1}\text{ yr}^{-1}$  (Heyman et al., 2016). Ages were calculated using the Expage calculator (Heyman et al., 2016; <http://expage.github.io/data/calculator/expage-201708.zip>). Internal uncertainties include error in blank, carrier mass, and counting statistics, while external errors also include production rate uncertainties. The Russian (BOG) and Mongolian (TUR) samples were collected in 2013 and 2014 respectively.

Sample ID	Group ID	LAT	LONG	Altitude	Sample depth	Topo. shielding	Quartz weight	Be carrier added	$^{10}\text{Be}/^{9}\text{Be}$	$\pm$	$10\text{Be}$ conc.	$\pm$	Age	Ext. $\pm$	Int. $\pm$
		DD	DD	m a.s.l.	cm		g		$\times 10^{-15}$	$\times 10^{-15}$	$\times 10^{-15}$	$\times 10^{-15}$	atoms $\text{g}^{-1}$	ka	ka
AL-13-C-017	BOG2	49.7705	89.4039	2433	3.0	1.000	38.301	0.287	1981	38	967902	21715	32.6	1.9	0.7
AL-13-C-018	BOG2	49.7791	89.4057	2475	2.5	0.999	42.091	0.284	3497	65	1557107	33430	50.5	2.9	1.1
AL-13-C-019	BOG2	49.7688	89.4062	2447	3.5	0.998	41.100	0.288	1023	22	456885	11505	15.6	0.9	0.4
AL-13-C-020	BOG2	49.7553	89.4125	2444	3.0	0.999	55.180	0.286	2250	41	764187	16346	25.7	1.5	0.6
AL-13-C-013	BOG1	49.7539	89.4319	2554	2.8	0.999	41.592	0.281	3791	54	1710492	29688	52.5	3.0	0.9
AL-13-C-014	BOG1	49.7541	89.4319	2539	2.5	1.000	40.735	0.287	942	24	439805	11930	14.0	0.8	0.4
AL-13-C-015	BOG1	49.7526	89.4313	2559	3.0	1.000	43.956	0.288	1577	21	670284	11755	20.8	1.2	0.4
AL-13-C-016	BOG1	49.7596	89.4311	2519	2.5	0.999	39.459	0.288	2235	35	1066988	20271	33.6	1.9	0.6
AL14-01	TUR2	49.9478	89.9214	2289	2.0	1.000	42.343	0.217	3461	70	1184091	26768	43.7	2.5	1.0
AL14-02	TUR2	49.9483	89.9222	2284	2.0	1.000	15.066	0.222	1202	21	1182434	23796	43.8	2.5	0.9
AL14-03	TUR2	49.9481	89.9224	2280	2.0	1.000	23.611	0.266	1706	29	1280756	25431	47.6	2.7	1.0
AL14-04	TUR2	49.9487	89.9222	2280	2.5	1.000	56.367	0.272	4660	62	1499725	24995	56.1	3.2	0.9
AL14-05	TUR2	49.9489	89.9226	2281	2.0	1.000	32.484	0.266	2240	41	1225292	25645	45.5	2.6	1.0
AL14-06	TUR1	49.9569	89.9152	2126	2.0	1.000	2.708	0.280	77	5	486224	36803	20.6	1.9	1.6
AL14-07	TUR1	49.9569	89.9152	2126	2.0	1.000	23.780	0.285	781	27	620068	22408	26.2	1.7	1.0
AL14-08	TUR1	49.9560	89.9136	2120	2.0	1.000	28.097	0.286	912	29	616203	21023	26.1	1.7	0.9
AL14-09	TUR1	49.9560	89.9134	2121	2.0	1.000	28.085	0.287	775	16	523810	12139	22.3	1.3	0.5
AL14-10	TUR1	49.9553	89.9124	2126	2.0	1.000	35.606	0.288	821	24	439480	13801	18.7	1.2	0.6

the standard deviation"; Ross, 2003; see [supplementary dataset](#)). We assume that exposure age scatter that cannot be explained by measurement uncertainty is caused by either prior exposure before incorporation of the boulder into the glacial landform or post depositional processes that result in an incomplete exposure, or a combination of both. Both the exposure age, and the spread in exposure ages, of individual glacial landforms provide important information about glacial and post-glacial processes. To assess the clustering of exposure ages we calculate both the reduced chi-square statistic ( $\chi^2_R$ , Balco, 2011) and sigma-to-mean ratios ( $\sigma/X_m$ , Blomdin et al., 2016b). Both statistics tell us about the spread in a population and how well clustered the data is. For our poorly-clustered deglaciation ages we calculated the median and indicate the interquartile range. We also examine the spread in ages by computing normal probability density estimates of the ages and internal uncertainties of the  $^{10}\text{Be}$  sample groups (cf. Lowell, 1995). The cosmogenic nuclide sample information is summarized in [Table 1](#), while additional information on the boulder samples is provided in the [supplementary data](#). We also perform boulder erosion sensitivity tests on our calculated deglaciation ages, using erosion rates of 1, 3, and 5 mm  $\text{kyr}^{-1}$  ([Fig. 9](#)). These rates have been used previously in the Tian Shan (Koppes et al., 2008). When zero-erosion deglaciation ages are discussed they should be regarded as minimum deglaciation ages of moraine surfaces. We omit corrections for snow cover and vegetation changes in our calculations as we don't have constraints on these and as they are commonly assumed to have limited effect on exposure ages (e.g. Gosse and Phillips, 2001).

Finally, we compare our data from the Ikh Turgen mountains with other  $^{10}\text{Be}$  exposure age datasets from the northern sectors of High Asia, centered on the Altai Mountains (Reuther, 2007; Gribenski et al., 2016; 2018; Ganyushkin et al., 2018), but also including the Tian Shan (Blomdin et al., 2016b; Tian Shan compilation, 2005–2015; new data from Li et al., 2016; Zhang et al., 2016), the Karlik Range (Chen et al., 2015), the Khangai Mountains (Rother et al., 2014; Smith et al., 2016), the Gobi-Alтай region (Batbaatar et al., 2018), the Eastern Sayan Mountains (Gillespie et al., 2008; Arzhamnikov et al., 2012; Batbaatar and Gillespie, 2016), and the southern part of the Baikal region (Horiuchi et al., 2004) ([Fig. 1](#)). We extract these datasets from the Expage database ([www.expage.github.io/](http://www.expage.github.io/); Version expage-201803). When analysing the  $^{10}\text{Be}$  data, we adopt the approach developed by Heyman (2014) and Blomdin et al. (2016b) and divide our  $^{10}\text{Be}$  exposure ages into confidence classes (A–C) based on simple statistics, such as  $\chi^2_R$  and  $\sigma/X_m$ , to ensure robust spatial and temporal correlations (data evaluation is summarized in the [supplementary data](#)). These confidence classes are defined as (Blomdin et al., 2016b):

1. Class A (well-clustered),  $\chi^2_R \leq 2$ .
2. Class B (moderately-clustered),  $\chi^2_R > 2$ ,  $\sigma/ < 15\%$ .
3. Class C (poorly-clustered),  $\chi^2_R > 2$ ,  $\sigma/X_m \geq 15\%$ .

Sample group divisions are also extracted from the Expage database, only considering groups with  $n \geq 3$   $^{10}\text{Be}$  samples. When sample groups for the Tian Shan compilation (including studies by Hubert-Ferrari et al., 2005; Koppes et al., 2008; Kong et al., 2009; Li et al., 2011, 2014; Zech, 2012; Lifton et al., 2014a) in Blomdin et al. (2016b) differ from the classification by the Expage, we indicate this and provide a comment in the [supplementary data](#). To warrant the consistency in our comparison we have recalculated all previously published ages using the methods stated above.

### 3.3. Geomorphometric analysis

To compare the topographic context of glaciation in the Boguty and Turgen-Asgat catchments, we compute a curvilinear swath profile (Telbisz et al., 2013) by calculating the minimum (valley floor), and maximum (highest peak) elevations along cross-catchment transects

(25 m grid step) perpendicular to a swath mid-line which runs between the respective maximum traces of glacial deposits on each side of the Ikh Turgen mountains ([Fig. 3e](#)). For a better visualization of the cross catchment transects, they have been rarified in [Fig. 3e](#). This calculation is performed in a GIS environment using the SRTM DEM 30 ( $30 \times 30$  m per pixel) and is implemented for both the total catchment topography and for the extracted moraine and hummocky terrain topography. From this analysis, we can extract differences in the catchment geometries, and use these to evaluate the style and extent of glacial deposition, which are important for inferring paleoglacier dynamics. Complementing this analysis, we calculate hypsometric distributions (i.e. histograms of the frequency of DEM pixels (area) in different elevation bins), using the SRTM DEM 90 ( $90 \times 90$  m per pixel; also extracted from <https://earthexplorer.usgs.gov/>), for the total catchment topography, and for the moraine, hummocky terrain, and glacier topography using 25 m elevation bins (Brozovic et al., 1997; Brocklehurst and Whipple, 2004).

To infer topoclimatic differences between the Boguty and Turgen-Asgat catchments we plot the variations in the July/January mean temperatures and precipitation sums ( $\sim 1950$ –2000) along the swath-mid line for the two catchments. These data were derived from the WorldClim dataset (<http://www.worldclim.org>), which is generated by interpolating monthly climate data from weather stations on an equidistant grid with the resolution of  $1 \times 1$  km (Hijmans et al., 2005). The temperature and precipitation data are also calculated along cross-catchment transects, perpendicular to the swath mid-line ([Fig. 3e](#)).

Finally, we use a simple 2-D ice surface profile model to estimate whether the paleoglaciers in the Boguty and Turgen-Asgat catchments were connected (sharing ice divides) as an ice field. We use an Excel spreadsheet tool, developed by Benn and Hulton (2010), to calculate ice surface profiles assuming perfect plasticity of the ice. The tool calculates the ice elevation along the bed topography of the glacier flow-line (minimum elevation along the swath mid-line, for each cross-catchment transect in [Fig. 3e](#)) and only requires an input of the yield stress, which is assumed to describe the basal shear stress regime of a glacier and a shape factor (accounting for the valley-drag effects). We calculated profiles using a 25 m grid step and assuming a constant basal shear stress of 50 and 100 kPa at the glacier's base. The adopted range of yield stress values is broadly consistent with the inferences of Li et al. (2012) for five present-day glaciers in northwest China. Outside the main mountain fronts on each flank of the massif, a shape factor of 1 was used because there are no valley-drag effects. In the part of the profile upstream from the mountain fronts, a shape factor of 0.5 was used for both Boguty and Turgen-Asgat. These were estimated from average shape factors calculated for several cross sections throughout the catchment.

## 4. Results

### 4.1. Glacial geomorphology

The Boguty catchment has a total area of  $249 \text{ km}^2$ , with an average elevation of 3009 m a.s.l. and an elevation range of 1562 m between the lowest point of the catchment (2236 m a.s.l.) and the highest peak (3798 m a.s.l.) ([Fig. 4](#)). Two tributary valleys about 15 km long and with distinct glacial cross-sections (U-shaped) terminate at the mountain front ([Fig. 4](#)). Towards the terminal areas the catchment long-profile becomes flatter and the interfluves and valley floor are draped with glacial sediment. The maximum extent of glaciation in the Boguty catchment is represented by large areas of moraine complexes and hummocky terrain, deposited distal to the two trunk valleys and extending across the lower-lying terrain ([Fig. 4b](#)). The moraine complexes at the most distal part of the catchment ([A] and [B] in [Fig. 4b](#)) contain distinct ridges but the most extensive glacial deposition consists of hummocky terrain ([C] in [Fig. 4b](#)) and lacks clear ridge morphology. Up valley, the ridge complexes become less well defined and grade into

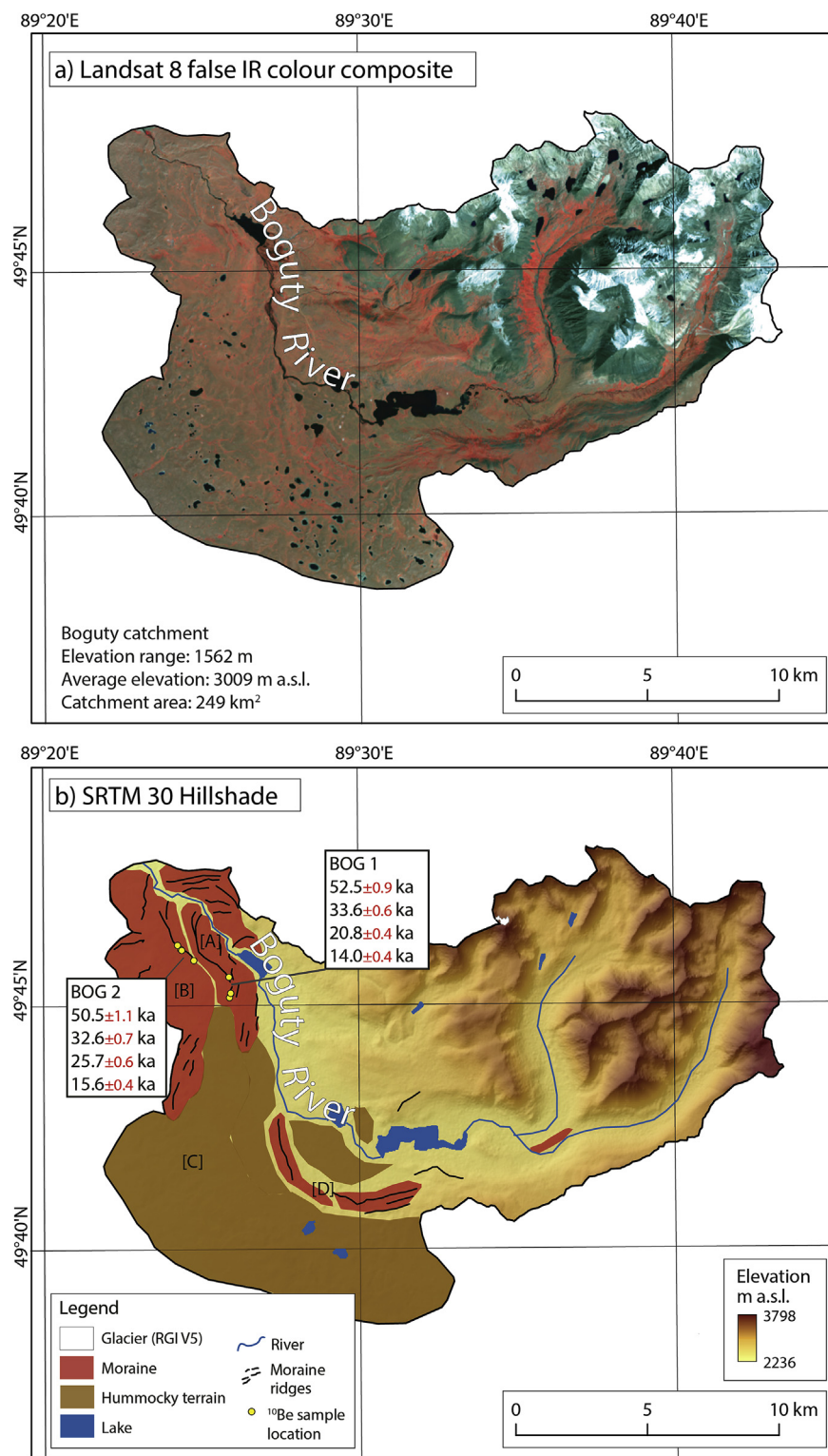


**Fig. 4.** Glacial geomorphology and sampling sites in the Boguty catchment, Ikh Turgen mountains. a) Landsat 8 false-IR colour composite and b) SRTM 30 Hillshade, glacial geomorphology, and cosmogenic sample locations. See Fig. 3 for location of the Boguty catchment and Table 1 for cosmogenic nuclide sample information. Letters [A], [B], [C] and [D] in Fig. 3b refers to landforms discussed in the main text. (For interpretation of the references to colour in this figure legend, the reader is referred to the Web version of this article.)

the hummocky terrain. Closer to the mountain front, there are sections of moraine complexes containing multiple moraine ridges indicating several ice-marginal positions [D] in Fig. 4b). Whether these systems of moraine ridges are recessional moraines or representative of a repeated glacier re-advances is difficult to infer.

The Turgen-Asgat catchment has a total area of 261 km<sup>2</sup>, with an average elevation of 2864 m a.s.l. and an elevation range of 1929 m between the lowest point of the catchment (1910 m a.s.l.) and the highest peak (3839 m a.s.l.) (Fig. 5). One long glacially-eroded trunk valley stretches for about 30 km from south to northeast until it reaches

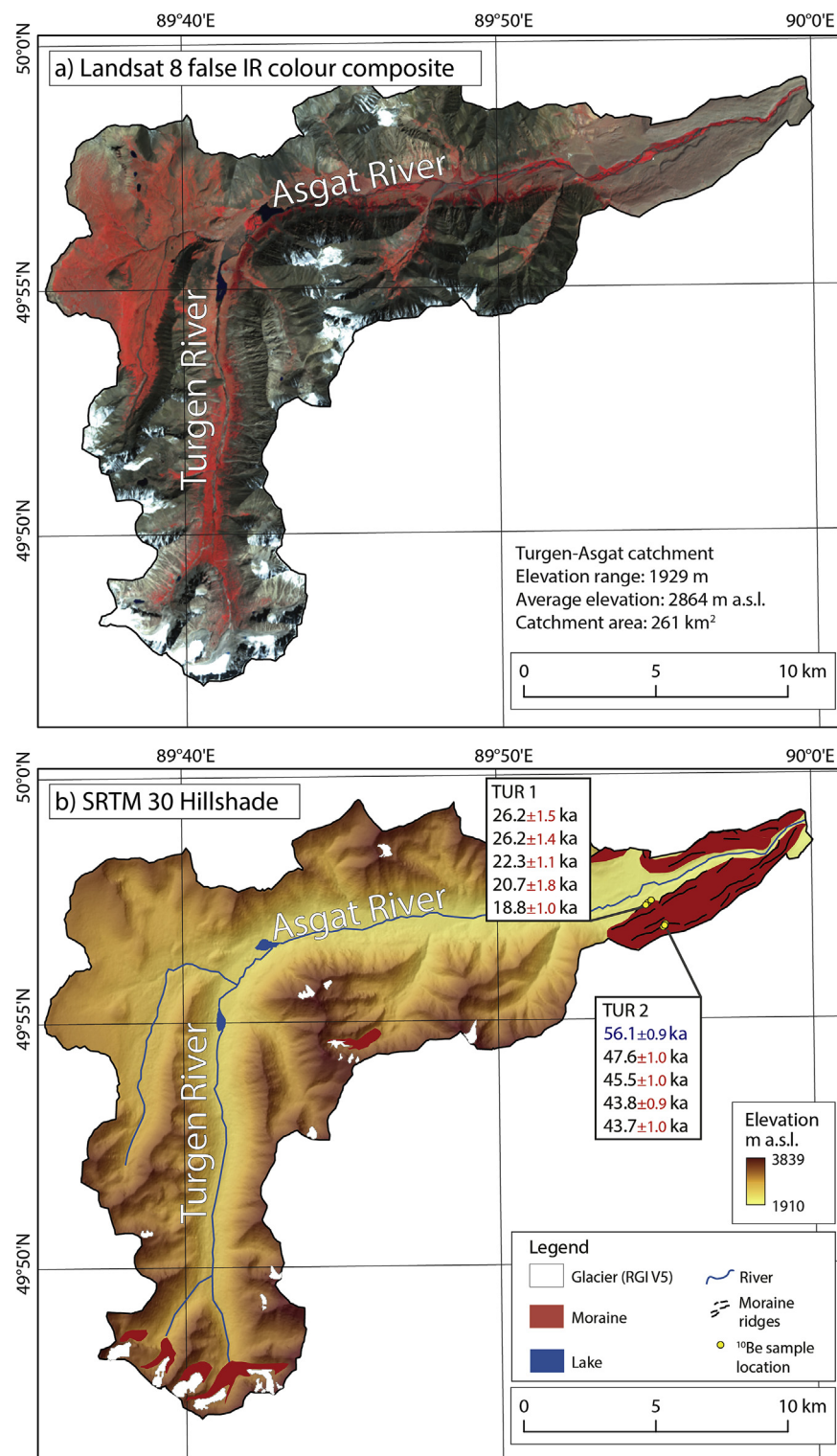


**Fig. 5.** Glacial geomorphology and sampling sites in the Turgen-Asgat catchment, Ikh Turgen mountains. a) Landsat 8 false-IR colour composite and b) SRTM 30 Hillshade, glacial geomorphology, and cosmogenic sample locations. A blue  $^{10}\text{Be}$  surface exposure age indicates an outlier rejected from the mean moraine age. See Fig. 3 for location of the Turgen-Asgat catchment and Table 1 for cosmogenic nuclide sample information. (For interpretation of the references to colour in this figure legend, the reader is referred to the Web version of this article.)

the mountain front (Fig. 3c). The maximum extent of glaciation on the eastern flank of the Ikh Turgen is marked by a large latero-frontal moraine complex extending ~10 km beyond the valley mouth (Fig. 5b). The glacial till of this feature is deposited on top of an older alluvial fan surface (Fig. 3c); and the boundary between the till and the fan is clearly visible in the Landsat 8 imagery (Fig. 3a). During field

inspection we confirmed the absence of glacial erratics on the fan. The latero-frontal moraine is elevated ~150 m above the valley floor and has multiple inset ridges (Fig. 5b). There is also evidence that a glacier overrode the left-lateral section of the complex depositing a terminal moraine north-eastward of the main valley orientation (Fig. 3c). The left-lateral section of the latero-frontal moraine shows a wide erosional

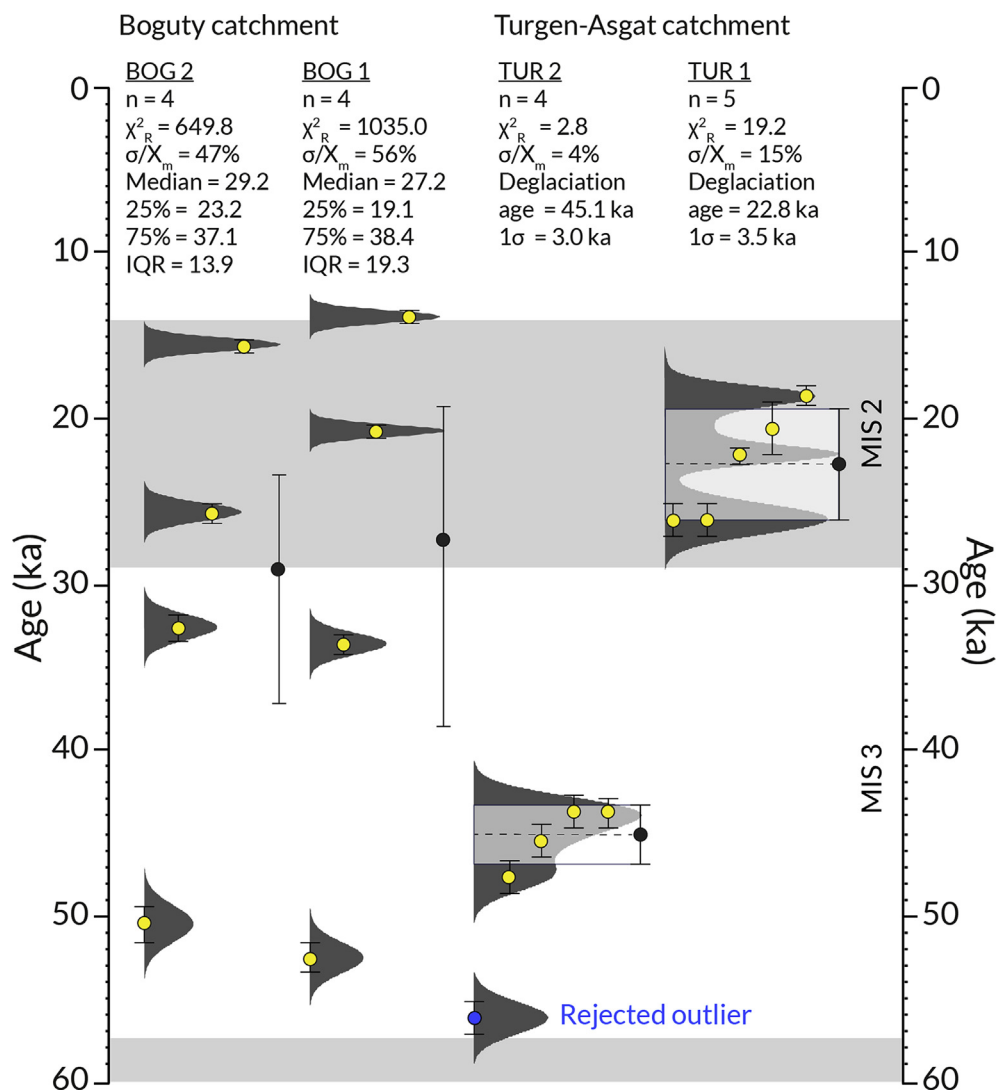


**Fig. 6.** Glacial chronology of the Ikh Turgen mountains. The large scatter of individual  $^{10}\text{Be}$  ages for BOG 2 and BOG 1 is illustrated by calculating the median surface exposure age and interquartile range (IQR). The deglaciation ages of the TUR 2 and TUR 1 moraines are represented by the arithmetic mean age and standard deviation ( $1\sigma$  + production rate uncertainties added in quadrature), after outlier rejection (blue circle) in the TUR 2 case. Also shown are exposure age statistics and normalized probability density estimates, calculated using internal errors. Marine oxygen isotope stages (MIS) adopted from Lisiecki and Raymo (2005). (For interpretation of the references to colour in this figure legend, the reader is referred to the Web version of this article.)

gap indicating that a paleoglacier expanded out of a southern tributary valley, eroded this section of the left-lateral and subsequently deposited a terminal moraine. The main trunk valley lacks visible moraine ridges, except for recently deposited moraines in association with the modern glacier fronts (Fig. 5b). Moraine deposits associated with modern glacier termini are also present in the tributary valleys to the main trunk valley (Fig. 5b). A strike-slip fault runs along the eastern flank of the mountain front (Fig. 3b); resulting in the eastern moraine complexes appear to have been offset slightly towards the south.

#### 4.2. $^{10}\text{Be}$ surface exposure ages

**Boguty catchment.** Our  $^{10}\text{Be}$  samples were collected from granitic boulders deposited on the lateral sections of two moraine ridges that are part of the two most distal moraine complexes (supplementary data; Fig. 4b). We sampled four boulders from each of two distinct crests (BOG 1 and BOG 2) that are clearly visible in the Landsat 8 imagery (Fig. 4a and b). The  $^{10}\text{Be}$  surface exposure ages in the Boguty catchment display large scatter. Morpho-stratigraphically, BOG 2 should be older than BOG 1 but the two landforms yield indistinguishable age populations, ranging between 14 and 53 ka (Fig. 6, Table 1). Both boulder groups exhibit poor exposure age statistics. BOG 2 has a  $\chi^2_R = 650$  and  $\sigma/X_m = 47\%$ , while BOG 1 has a  $\chi^2_R = 1035$  and  $\sigma/X_m = 56\%$  (Fig. 6, supplementary data).

**Turgen-Asgat catchment.** Our  $^{10}\text{Be}$  samples were taken from granitic

boulders deposited on the upper part of the southern latero-frontal moraine complex (TUR 2), and from the innermost of a series of inset moraine ridges (TUR 1) (supplementary data; Fig. 5b). The latero-frontal moraine complex and inset moraine ridges are clearly visible in the Landsat 8 imagery (Fig. 5a). We sampled 5 boulders from each moraine crest. The  $^{10}\text{Be}$  surface exposure ages show a moderate degree of scatter (supplementary data). The five boulders from TUR 2, the flat upper part of the lateral section, range in age from  $43.7 \pm 1.0$  ka to  $56.1 \pm 0.9$  ka (Fig. 6, Table 1); the oldest exposure age was rejected using Peirce's criterion. The four remaining  $^{10}\text{Be}$  surface exposure ages are relatively-well clustered, with  $\chi^2_R = 2.8$  and  $\sigma/X_m = 4\%$  and provide a mean deglaciation age of  $45.1 \pm 3.0$  ka (Fig. 6). Five boulders from the innermost of several right-lateral inset moraine ridges range in age between  $18.7 \pm 0.6$  ka and  $26.2 \pm 1.0$  ka. TUR 1 has a  $\chi^2_R = 19.2$ ,  $\sigma/X_m = 15\%$ , and a mean deglaciation age of  $22.8 \pm 3.5$  ka (Fig. 6). Taken together, the apparent deglaciation ages indicate extensive glacier expansion beyond the eastern mountain front during MIS 3 and MIS 2.

#### 4.3. Geomorphometric analysis

The curvilinear swath profile, reconstructed ice surface profiles (Fig. 7) and hypsometric analyses (Fig. 8) allow for several observations:

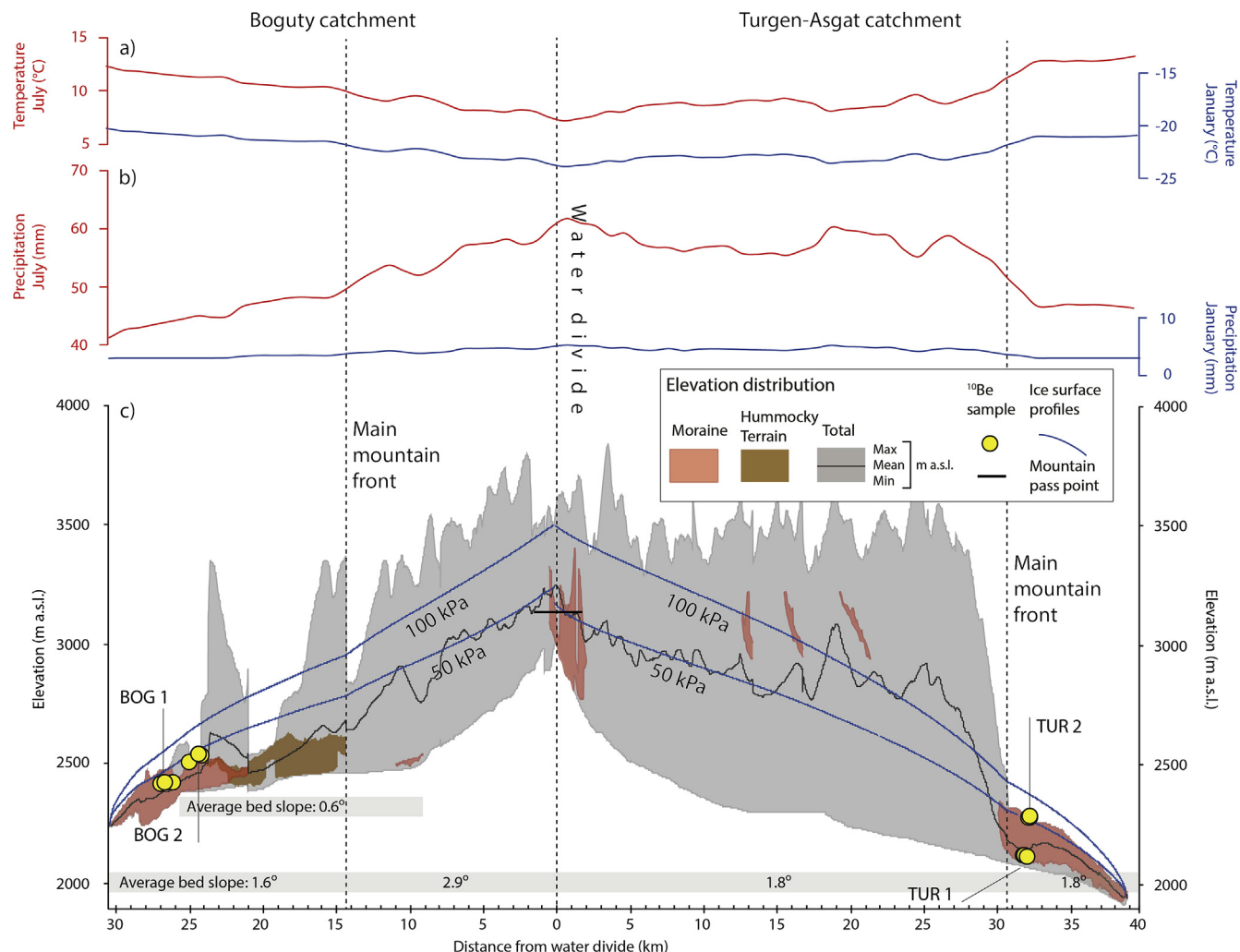


**Fig. 7.** a and b) Presents day climatic setting and paleoglaciological dynamics. a) Averaged ~1950–2000 (interpolation of observational data) mean air temperature and total precipitation during July and January (Hijmans et al., 2005) and c) curvilinear swath profile showing maximum, mean, and minimum elevations of the two investigated catchments, elevation distribution for glacial landforms (moraines and hummocky terrain), and reconstructed ice surface profiles with uniform 50 kPa and 100 kPa basal shear stresses using the approach of Benn and Hulton (2010). Also shown are average bed slopes across different sections. Fig. 3e illustrates the location of the swath mid-line, cross-valley transects (25 m spacing), and extent of the analysed catchment. Note that the moraines in the mid-section of the Turgen-Asgat catchment are located high up in tributary valleys close to small glaciers.

- Based on the elevation distribution of glacial landforms we infer that the Boguty paleoglacier extended ~30 km down valley to an altitude of ~2240 m a.s.l. and the Turgen-Asgat paleoglacier extended ~40 km down valley to an altitude of ~1940 m a.s.l. (Fig. 7c).
- Most of the Boguty catchment area is concentrated at ~2500 m a.s.l. (~30 km<sup>2</sup>), coinciding with where most moraine and hummocky terrain is located (Fig. 8a). Turgen-Asgat, on the other hand, has a higher proportion of the catchment area at higher elevations between 2700 and 3200 m a.s.l. (~150 km<sup>2</sup>) (Fig. 8b). This elevation difference drives important topoclimatic differences between the two catchments. These differences are illustrated in the contemporary temperature and precipitation data, as the Boguty catchment has lower total precipitation and overall higher air temperatures compared to the Turgen-Asgat catchment (Fig. 7a and b). The differences in precipitation and temperature also seem coupled with the potential size difference of the Boguty and Turgen-Asgat paleoglacier accumulation areas (~222 and 257 km<sup>2</sup> respectively; Fig. 8), resulting in potentially more extensive accumulation areas for the Turgen-Asgat catchment.
- A larger distance between the outermost glacial deposit and the mountain front exists in Boguty in comparison to the Turgen-Asgat catchment. The fraction of the Boguty paleoglacier that was topographically constrained (i.e. constrained by the valley slopes before reaching the mountain front) equalled only 50% of its maximum length, in contrast with 75% inferred for the Turgen-Asgat paleoglacier (Fig. 7c).
- The average bed slope of the Boguty catchment is higher in gradient (2.9°) than that of the Turgen-Asgat catchment (1.8°), however Boguty has notably flatter sections down valley (Fig. 7c). The bed topography of the two catchments, together with the glacier lengths and shape factors, impacts the 2-D ice surface profile reconstruction. The Boguty paleoglacier was thinner than the Turgen-Asgat paleoglacier (Fig. 7c), assuming a constant basal shear stress (either 50 or 100 kPa).
- Regardless of basal shear stress applied (either 50 or 100 kPa), the ice surface profile reconstruction indicates the possibility that the Boguty and Turgen-Asgat paleoglaciers shared an ice divide and belonged to an ice field-style glacier system (Fig. 7c).

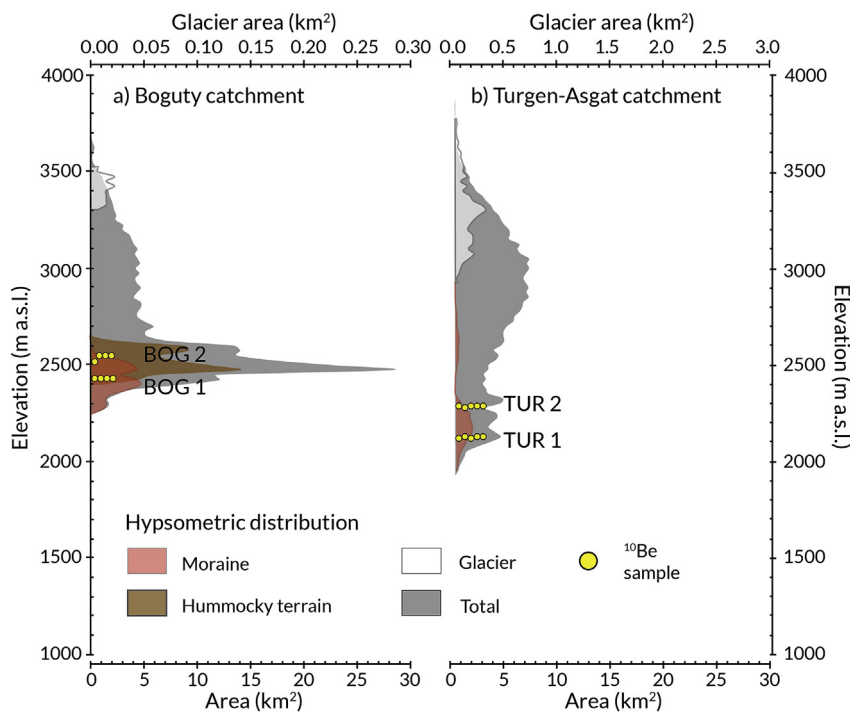


**Fig. 8.** Hypsometric distributions of moraine, hummocky terrain, glacier, and total catchment topography for a) the Boguty and b) the Turgen-Asgat catchments. Also shown is the elevation of  $^{10}\text{Be}$  samples. The hypsometric distributions are histograms and elevations are summed in 25 m bins.

#### 4.4. Regional comparison

A comparison between the Ikh Turgen  $^{10}\text{Be}$  glacial chronology (Fig. 6) and other  $^{10}\text{Be}$  chronologies from the Altai, Khangai, Karlik, Gobi-Altaï, eastern Sayan, south Baikal and the Tian Shan shows that most well-constrained datasets overlap with MIS 2 (supplementary data; Fig. 9). In Fig. 9 all  $^{10}\text{Be}$  data from the northern sector of High Asia are sorted into three classes based on degree of clustering/robustness (A–C confidence classes). The well- and moderately-clustered groups (A and B) have a similar averaged relative uncertainty and constitute 38% of the dataset, compared with the 62% of poorly-clustered data (supplementary data; Fig. 9). Using only the well and

moderately constrained data, the deglaciation age of TUR 2 partly overlaps with two MIS 3 deglaciation ages from the Tian Shan dataset (Li et al., 2014; Zhang et al., 2016), whereas TUR 1 generally coincides with the timing of glaciation during MIS 2 (Fig. 9). The poor exposure-age statistics of BOG 2 and BOG 1 prohibit a proper comparison to other glacial chronologies of the region (Fig. 9). However, the large exposure age scatter of BOG 2 and BOG 1 (resulting in large deglaciation age error bars) is typical of exposure ages obtained across the northern sector of High Asia (Fig. 9).

Fig. 9 also shows the sensitivity of deglaciation ages to boulder erosion rates. The influence of erosion on deglaciation ages younger than 30 ka is negligible; erosion rates of 1, 3 and 5 mm  $\text{kyr}^{-1}$  produce

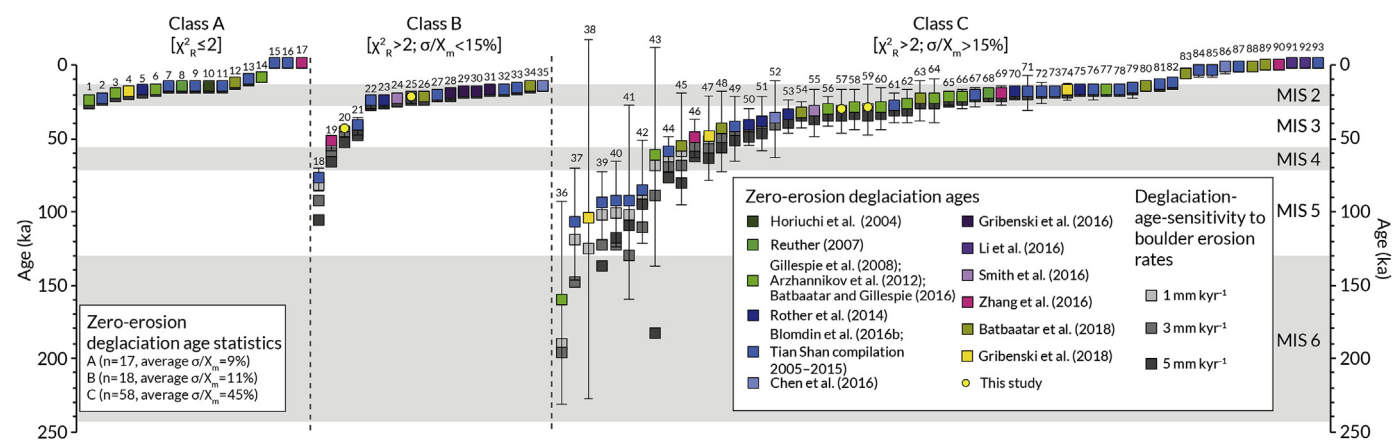


**Fig. 9.** Moraine deglaciation ages and their sensitivity to boulder erosion rates (1, 3 and 5 mm  $\text{kyr}^{-1}$ ), across the northern sector of High Asia, including the Tian Shan (only  $^{10}\text{Be}$  sample groups with  $n \geq 3$ ). Numbers refer to Group IDs listed in the supplementary data. The Tian Shan compilation of Blomdin et al. (2016b) includes  $^{10}\text{Be}$  glacial chronologies published during the period of 2005–2015 (Hubert-Ferrari et al., 2005; Koppes et al., 2008; Kong et al., 2009; Li et al., 2011; 2014; Zech, 2012; Lifton et al., 2014a). The exposure age class criteria are taken from Blomdin et al. (2016b). Details of the data analysis are given in the supplementary data. Note that exposure ages that become saturated after adopting boulder erosion rates are excluded from the analysis. This may lead to groups having less than 3 samples and then becoming excluded in our data analysis (e.g. #36–38). In other cases, saturated samples are excluded, leading to reduced number of exposure age samples in a group. This causes calculated deglaciation ages, accounting for 5 mm  $\text{kyr}^{-1}$  of boulder erosion, to become younger than their equivalents accounting 3 mm  $\text{kyr}^{-1}$  (e.g. #40–42).

an average age increase of 3%, 8% and 13%, respectively. Samples with longer exposures, between 30 and 50 ka, are increasingly sensitive to erosion; erosion rates of 1, 3 and 5 mm kyr<sup>-1</sup> result in average age increases of 5%, 14% and 22%, respectively. Class C age changes of this magnitude could complicate association of deglaciation ages with climate drivers associated with the marine isotope stages. Finally, for deglaciation ages between 50 and 100 ka, even small boulder erosion rates have an impact, increasing ages with 10%, 29% and 49% for 1, 3 and 5 mm kyr<sup>-1</sup>, respectively. Note, that for the oldest deglaciation ages in the dataset taken from the literature, adopting high enough boulder erosion rates may result in a sample being saturated.

## 5. Discussion

### 5.1. Extent of glaciation

We have mapped and identified the maximum extent of past glaciation in the Ikh Turgen mountains. Our mapping focused on distinguishing individual ridge crests in the Landsat 8 imagery, but we also modified the extent of larger moraine complexes mapped by Blomdin et al. (2016a) (Fig. 3c, 4 and 5). This modification is based on a combination of field observations and new examination of the Landsat 8 imagery. In general, the extent of moraines presented in this study is slightly larger than those presented in the moraine dataset of Blomdin et al. (2016a). The break of slope between the glacial sediment and the surrounding alluvial fan sediment (on the eastern flank) and weathered soils is clearly distinguishable in the Landsat 8 imagery. During field-work, we also noted the absence of erratic boulders outside the limits of clearly identified glacial sediment. Our minimum estimate of maximum glaciation (aerial extent), illustrated in Fig. 3c, is based on these well-defined limits and broadly overlaps with the reconstructions by Lehmkuhl et al. (2004) and Blomdin et al. (2016a). Four main valley paleoglaciers drained the eastern part of the Ikh Turgen mountain and on the western side paleoglaciers coalesced to form two separate ice lobes rather than multiple valley outlet glaciers (Fig. 3d).

We conclude that the paleoglaciers in the Boguty and Turgen-Asgat catchments extended over ~30 and ~50 km down valley to altitudes of

~2240 m a.s.l. and ~1940 m a.s.l., respectively (Fig. 7). Other large valley glaciers existed in the past in the Altai Mountains, including the Chuya Basin to the west and the Turgen-Kharkhira Mountains to the east (Fig. 2). For example, the Chagan-Uzun moraine complex in the western part of the Chuya Basin (Fig. 2) was formed by a paleoglacier extending over ~55 km down valley to an altitude of ~1900 m a.s.l. (Gribenski et al., 2016) and paleoglaciers draining the Turgen-Kharkhira Mountains extended ~30 km down valley and deposited large moraine complexes at altitudes of 1950–2250 m a.s.l. (Lehmkuhl et al., 2004). Paleoglaciers draining these mountains and Ikh Turgen extended beyond the confines of individual valleys and developing a chronology for deglaciation, using glacially deposited landforms, is crucial for understanding the glacial history of the Ikh Turgen mountains.

### 5.2. Timing of glaciation

We have established a glacial chronology for the Turgen-Asgat moraines using <sup>10</sup>Be surface exposure dating. Our working hypothesis was that glacial retreat on either side of the divide would be coeval but the spread in surface exposure data on the western side of the mountain precludes establishing deglaciation ages in the Boguty catchment.

**Boguty catchment.** Surface exposure ages from two moraine crests have ages ranging from 14 to 53 ka. All samples were from granitic boulders that likely came from the upper part of the catchment where felsic plutonic rocks have been mapped (Fig. 3b). The sampled moraine crests are distinct, and we mapped the nearest surrounding sediment as belonging to the moraine complex. The calculated ages are scattered and do not indicate a single geologic event; associating the mean with deglaciation is not appropriate (cf. Heyman et al., 2011). Boulder erosion is unlikely to be the cause of the scatter in ages. All the boulders have the same granitic source and they have similar varnish and weathering patterns. It is more likely that the age scatter is the result of one or a combination of the following processes:

1. Incomplete exposure: deglaciation by melt-out of stagnant glacier ice resulting in post-glacial landform surface instability due to permafrost conditions and slow decay of glacial ice buried underneath a

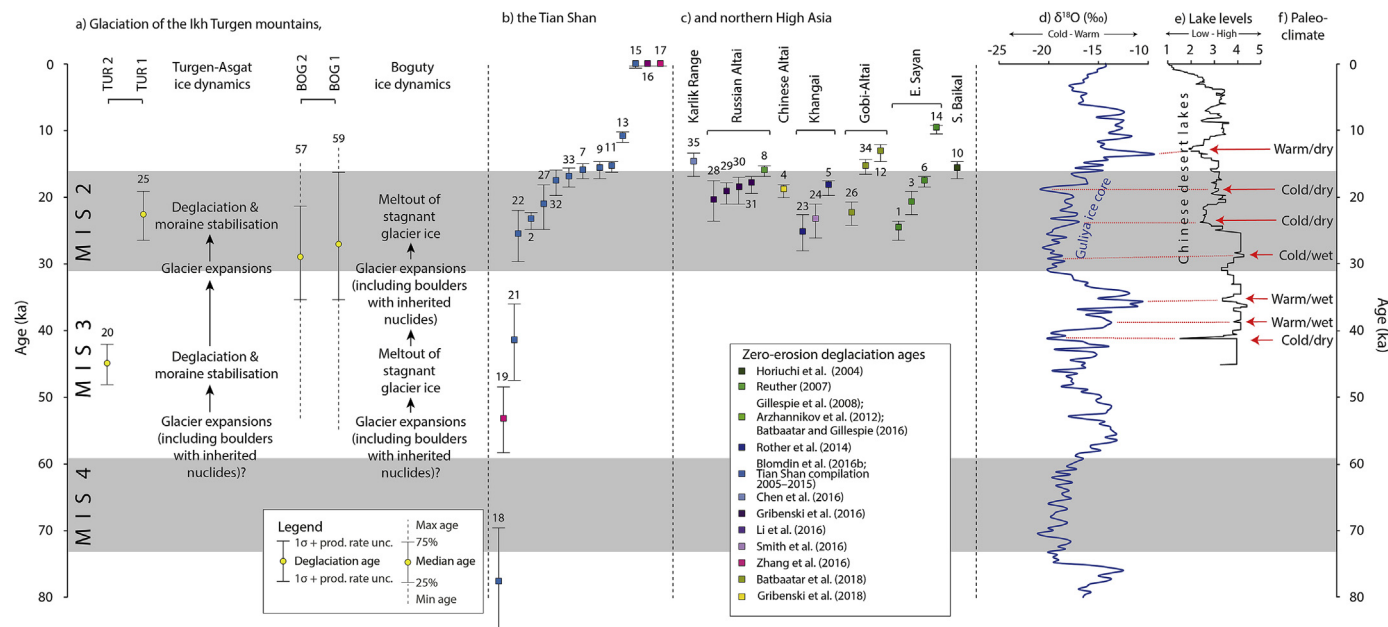


**Fig. 10.** a) Timing of glaciation of the Ikh Turgen mountains and interpreted glacier dynamics, b) timing of glaciation across the Tian Shan and c) the northern sector of High Asia. Only well and moderately clustered exposure age groups ( $n \geq 3$ ) have been considered (classes A and B; see Fig. 9). Numbers refer to Group IDs listed in the supplementary data. d) The Guliya ice core record from Kunlun Shan, northwestern Tibet (Thompson et al., 1997; see Fig. 1 for location), e) Lake level (water balance) records (1 = low; 5 = high lake levels) from northwestern China and Inner Mongolia (Wünnemann et al., 2007; see Fig. 1 for locations), and f) Paleoclimate inferred from proxy records. Marine oxygen isotope stages (MIS) adopted from Lisiecki and Raymo (2005).

surface moraine deposit (cf. Zech et al., 2005, Fig. 10a). The numerous ponds and lakes in the Boguty catchment supports this hypothesis.

2. Inheritance: deglaciation by debris-covered glaciers, including: supraglacially transported boulders with inherited nuclides, boulders with inheritance recycled from previous advances or from rock falls (cf. Putkonen and Swanson, 2003, Fig. 10a). There are however, no present-day debris-covered glaciers in the Ikh Turgen Mountains to evaluate the likelihood of this scenario.

3. Inheritance: due to the size of the moraine complexes, we suspect that the BOG 1 and BOG 2 ridges were formed by ice advancing over pre-existing sediment fills that had been trapped in the low-gradient forefield beyond the mountain front (average slope angle of 0.6°, Fig. 7c). An extensive forefield with negligible surface slope inhibited the Boguty paleoglaciers from excavating boulders from the substrate. The combination of few recently excavated boulders with no inheritance mixing with boulders having inherited  $^{10}\text{Be}$  Be plausibly produced an age distribution characterized by scatter (Fig. 10a).

The age scatter precludes an association of the deglaciation of the Boguty moraines to global forcing events.

*Turgen-Asgat catchment.* The surface exposure ages from the Turgen-Asgat catchment indicate that paleoglaciers expanded beyond the eastern mountain front during MIS 3 and MIS 2. These paleoglaciers produced a massive latero-frontal moraine complex. This is a common feature in glaciated high-alpine areas, and they are typically produced by paleoglaciers with thick debris mantles (c.f. Benn and Owen, 2002). Its large size ( $\sim 40 \text{ km}^2$  and  $\sim 150 \text{ m}$  thick; Figs. 7 and 8) and the presence of multiple inset ridges indicates that this landform might be composite in nature. The rejected old outlier on TUR 2 could be a boulder recycled from a previous advance or from a rock-fall (Putkonen and Swanson, 2003), and boulders are more likely to carry an inherited component in these type of moraine deposits (Benn and Owen, 2002). Comparisons of sample locations with the distribution of felsic plutonic rocks on the GLiM lithological map (Hartmann and Moosdorf, 2012), these boulders have either come from the upper parts of the catchments or from the local slopes of the mountain front (Fig. 3b). It is also possible that the rejected sample was derived from the local pluton shown in Fig. 3b, and that it thus contains inherited cosmogenic nuclides.

To add robustness to our reconstruction of the extent and timing of glaciation in the Ikh Turgen mountains, we explore the dynamics of these paleoglaciers using geomorphometric analysis.

### 5.3. Glacial dynamics

We have used two different methods for geomorphometric analysis (curvilinear swath profile and hypsometric analyses) and a simple 2-D ice surface reconstruction to compare and contrast the topographical context for paleoglaciuation in the Boguty and Turgen-Asgat catchments (Figs. 7 and 8). This approach has been motivated by the fact that topography exerts important controls on the deposition of moraines (Barr and Lovell, 2014). Our geomorphometric analysis reveals several factors that may have caused differences in the dynamics of paleoglaciuation in the two opposing catchments and might have affected the style of moraine deposition.

*Boguty catchment.* Compared with Turgen-Asgat, the paleoglaciers in the Boguty catchment have a lower potential for developing large accumulation areas ( $\sim 222 \text{ km}^2$ ); the hypsometry of the catchment (elevation concentrated at lower altitudes and less orographic precipitation) is less conducive to ice accumulation, the drainage is less topographically constrained and has flatter down valley sections (Figs. 7 and 8). Two paleoglacier branches merged at the mountain front before inundating a low-gradient forefield (Fig. 7). Our analysis suggests that basal shear stresses lower than the commonly inferred minimum value of 50 kPa (e.g., Li et al., 2012; Bræstrup et al., 2016) are required to match ice surface profiles to moraine elevations.

Previous studies have shown that lower values may occur under topographically unconstrained sections of glaciers moving on deformable sediment (cf. Glasser and Jansson, 2005; Eugster et al., 2016; Gribenski et al., 2016). Relatively low basal sliding velocities, typically associated with lower topographic gradients, imply that the Boguty paleoglaciers were ineffective in eroding and excavating pre-existing sediment in the lowlands (cf. Scherler et al., 2011). Modelling experiments show that the primary effect of repeated glaciation is to flatten a valley floor and to steepen its headwalls causing an erosional feedback on subsequent glacier expansion, reducing the size of the next paleoglacier (Anderson et al., 2012). This observation supports the hypothesis that the Boguty paleoglacier was inhibited from excavating the substrate (section 5.2). It is possible that the paleoglacier dynamics affected the style of moraine deposition. Widespread deposition by stagnant or slow-moving paleoglaciers across a low gradient forefield could explain the scatter in exposure ages on the western side of Ikh-Turgen.

*Turgen-Asgat catchment.* Compared with the Boguty, the Turgen-Asgat paleoglaciers have a higher potential for developing larger accumulation areas ( $\sim 257 \text{ km}^2$ ) at higher altitudes, were topographically constrained (down valley), and advance over steeper down valley sections. The topographic constraints on the Turgen-Asgat paleoglacier contributed to it becoming larger; it extended to lower altitudes than glaciers west of the water divide. Several advances of the Turgen-Asgat paleoglacier built the large latero-frontal moraine complex. The surface layer of the innermost inset moraine and the upper flat part of the latero-frontal moraine were both deposited during a minimum of two major advances and have deglaciation ages of  $22.8 \pm 3.5$  and  $45.3 \pm 2.7 \text{ ka}$ , respectively (Figs. 6 and 10). The deglaciation age uncertainties for these two surfaces may reflect the duration of moraine stabilization (cf. Briner et al., 2005, Figs. 6 and 10), or they may reflect variable exhumation and boulder erosion.

Our simple 2-D ice surface profile reconstruction, assuming a constant basal shear stress, indicates that the Boguty and Turgen-Asgat paleoglaciers potentially shared an ice divide and belonged to an ice field-style glacier system (Fig. 7). The lower parts of the two paleoglaciers have different topographic constraints that result in different dynamics. The assumption of a constant basal shear stress in the model is certainly a simplification, because in reality stress regimes at the base of glaciers are often found to be dissimilar in different glacier sections (Bræstrup et al., 2016; Sergienko and Hindmarsh, 2013). Yet, this approach provides first-order estimates for a range of possible ice-surface elevations (Benn and Hulton, 2010) and indicates different stress and flow regimes under glaciers on opposite flanks of the same mountain range.

### 5.4. Regional implications

Using a combination of remote-sensing based geomorphological mapping and geomorphometric analysis, we conclude that topographic/topoclimatic (local orographic precipitation effects) factors were responsible for different dynamic behaviours of paleoglaciers on opposite sides of Ikh Turgen Mountains.

In the Boguty catchment, the wide scatter of exposure ages prevents us from distinguishing individual deglaciation events, as well as linking our  $^{10}\text{Be}$  chronology to other proxy records (Fig. 10). Similar to previous studies, our results indicate that it is important to consider dynamics and topographic context in interpreting paleoglacial reconstructions (Scherler et al., 2011; Barr and Lovell, 2014), and that glacial chronological studies using cosmogenic nuclides should be aware of the difficulties involved when sampling complicated glacial landforms in complex catchments because these may produce a wide scatter in surface exposure ages. Alternate approaches for dating these types of moraine deposits might be, using larger sample populations, adopting multiple isotopes to infer burial/exposure histories of boulders, and/or applying other cosmogenic nuclide sampling

strategies, such as depth profile analysis. Fitting geomorphic process models to observed exposure age distributions has also previously shown promise in dealing with large scatter (Applegate et al., 2012).

The large scatter observed for the Boguty moraines is not in any way unique for the northern sector of High Asia (Fig. 9). Large moraine complexes in lowlands are tempting targets when reconstructing glacial chronologies since they represent the maximum extent of glaciation. Our results indicate it might be more suitable to target latero-frontal moraine complexes (cf. Turgen-Asgat) or simple lobate terminal moraines of maximum ice expansion inside valleys as these may yield more robust data. However, there are also problems of ‘obliterative overlap’ and self-censoring of the moraine record, which should be a smaller problem in the Boguty catchment, as glaciers occupying wide and unconfined basins are able to extend laterally when encountering obstacles (Gibbons et al., 1984; Kirkbride and Winkler, 2012).

In the Turgen-Asgat catchment, paleoglaciers retreated from their maximum positions at ~45 and ~23 ka. These deglaciation ages match other glacial and paleoclimate chronologies across the northern sector of High Asia. TUR 2 aligns with a plateau of low  $\delta^{18}\text{O}$  values in the Guliya ice core record (low temperatures; Thompson et al., 1997) and relatively high lake levels recorded across northwestern China and Inner Mongolia (Wünnemann et al., 2007) (Fig. 10). Glacier expansion during MIS 3 is supported by a cold and wet climate inferred from these paleoclimate records and is also consistent with the moderately-clustered deglaciation ages of Li et al. (2014); #21 in Figs. 9 and 10;  $41.6 \pm 5.7$  ka and Zhang et al. (2016); #19 in Figs. 9 and 10;  $53.4 \pm 4.9$  ka from the eastern Tian Shan (Fig. 10) and the poorly-clustered deglaciation age by Rother et al. (2014) from the Khangai (#50 in Fig. 9);  $41.9 \pm 12.9$  ka. Although, a persuasive MIS 3 glaciation signal has been difficult to correlate across High Asia (Gribenski et al., 2018), well-preserved moraines indicating MIS 3 glaciation seem to be located in largely drier continental regions (i.e. eastern Tian Shan, eastern Altai and the Khangai). The Zhang et al. (2016; MIS 3; #19 in Figs. 9 and 10) moraine was originally interpreted as an MIS 4 moraine (Zhang et al., 2016) and was not considered in the Gribenski et al. (2018) regional analysis. This discrepancy between the original (Zhang et al., 2016) and the new (this study) deglaciation age inferred for this site is likely an artifact of a combination of choice of reference production rates, different spallation production rates and differences in atmospheric pressure interpolation. In terms of reference production rates, Zhang et al. (2016) used the Northeast North American production rate of  $3.85 \pm 0.19$  atoms  $\text{g}^{-1}$  year $^{-1}$  (NENA, Balco et al., 2009), with the Lal (1991)/Stone (2000) scaling scheme, which accommodates paleomagnetic corrections (Nishiizumi et al., 1989), while this study uses a global production rate of  $3.98 \pm 0.25$  atoms  $\text{g}^{-1}$  year $^{-1}$  and LSD scaling (Lifton et al., 2014b; Heyman et al., 2016). It is also important to point out that, while the TUR 2 and the Li et al. (2014) MIS 3 deglaciation ages are robust for boulder erosion rates of up to  $5 \text{ mm kyr}^{-1}$  (in terms of MIS 3 overlap), the Zhang et al. (2016) deglaciation age is not and turns out to be MIS 4 in age when considering this erosion rate. Although both the TUR 2 moraine and Li et al. (2014) MIS 3 moraine were formed by large paleoglaciers extending beyond the confinement of their mountain fronts, a robust regional signal is still lacking (e.g. Gribenski et al., 2018).

We further compare the timing of the TUR 1 deglaciation and moraine stabilization with paleoclimate forcing and other glacial chronologies from the Tian Shan and northern High Asia (Fig. 10). Although the timing of TUR 1 aligns with an MIS 2 period of low  $\delta^{18}\text{O}$  values recorded in the Guliya ice core, it is also contemporary with low lake levels recorded across the region (Fig. 10). Inferred cold and wet conditions during early MIS 2 likely triggered glacier culmination but the transition to a drier climate resulted in more restricted paleoglacier extent than during MIS 3 (cf. Rother et al., 2014). This transition further triggered deglaciation of the TUR 1 moraine during MIS 2; and this interpretation is robust for erosion rates of up to  $10 \text{ mm kyr}^{-1}$  (Blomdin et al., 2016b). This sequence of events is consistent with other glacial

chronologies; several glacial events overlap within the MIS 2 boundaries and most of these MIS 2 moraines were formed by paleoglaciers restricted to their valleys (cf. Blomdin et al., 2016b). MIS 2 remains the most well recognized period of glacial expansion across the northern sector of High Asia.

## 6. Conclusions

- At their maximum extent, the larger Turgen-Asgat paleoglacier stretched ~40 km down valley to an altitude of ~1940 m a.s.l., the smaller Boguty paleoglacier stretched ~30 km down valley to altitude of ~2240 m a.s.l.
- In the Turgen-Asgat catchment, the deglaciation ages (minimum ages when not considering boulder erosion) of two moraine surfaces that are part of the same latero-frontal moraine complex are ~45 ka and ~23 ka. In the Boguty catchment, the deglaciation signal is obscured because of a large scatter among individual boulder ages.
- When the Turgen-Asgat and Boguty paleoglaciers were at their maximum extent they potentially shared an ice divide and belonged to the same glacier system. Although part of the same glacier system, they appear to have been dynamically different. Because of the hypsometry of its' catchment, the Turgen-Asgat paleoglacier, had higher potential to develop a larger accumulation area (~257 km $^2$ ), was mostly topographically constrained by a long trunk valley, and advanced across a relative steep bed down valley. In contrast, the hypsometry of the Boguty catchment, indicates that its paleoglacier likely had a smaller accumulation area (~222 km $^2$ ), concentrated at lower altitudes. When the Boguty paleoglacier expanded onto the lower lying terrain (unconstrained by valley topography) it advanced across a relatively flat bed.
- These differences had implications for the style of moraine deposition: deposition of widespread moraine complexes across the low-lying terrain in Boguty in contrast to the deposition of latero-frontal moraine in Turgen-Asgat.
- Deglaciation of the upper surface of the Turgen-Asgat lateral-frontal moraine complex coincides with MIS 3 and deglaciation of the innermost inset ridge coincides with MIS 2. The period before the MIS 2 deglaciation was characterized by colder and drier conditions and thus more limited glacier expansion than during the colder and wetter period prior to the MIS 3 deglaciation. Glacier culmination during MIS 2 is the most robustly dated glacial stage in northern High Asia.

## Acknowledgments

We would like to acknowledge financial support from the Swedish Research Council (No. 2011-4892) to Stroeven and the National Geographic Society to Harbor and Lifton (Grant 9073-12), as well as additional support for field studies from the Swedish Society for Anthropology and Geography (SSAG) and the Margit Alhtin and Carl Mannerfelt foundations to Blomdin and Gribenski. PRIME Lab, Caffee, and Lifton acknowledge support from NSF (EAR-1560658). Tom Clifton and Greg Chmiel are acknowledged for their help at Prime Lab during  $^{10}\text{Be}$  sample preparation and processing. We thank Valeria Kirejenko and Ivan Sobyanin for field assistance in 2013 and Adam Stjärnljus and Joakim Ojanen for field assistance in 2014. Alessa Geiger and one anonymous reviewer are acknowledged for their thorough and constructive reviews.

## Appendix A. Supplementary data

Supplementary data related to this article can be found at <http://dx.doi.org/10.1016/j.quageo.2018.05.008>.

## References

- Agatova, A.R., Nepot, R.K., 2017. Pleistocene glaciations of the SE Altai, Russia, based on geomorphological data and absolute dating of glacial deposits in Chagan reference section. *Geochronometria* 44, 49–65. <https://doi.org/http://dx.doi.org/10.1515/geochr-2015-0059>.
- Anderson, R.S., Dünforth, M., Colgan, W., Anderson, L., 2012. Far-flung moraines: exploring the feedback of glacial erosion on the evolution of glacier length. *Geomorphology* 179, 269–285. <https://doi.org/10.1016/j.geomorph.2012.08.018>.
- Applegate, P.J., Urban, N.M., Keller, K., Lowell, T.V., Laabs, B.J.C., Kelly, M.a, Alley, R.B., 2012. Improved moraine age interpretations through explicit matching of geomorphic process models to cosmogenic nuclide measurements from single landforms. *Quat. Res.* 77 (2), 293–304. <https://doi.org/10.1016/j.yqres.2011.12.002>.
- Arendt, A., Bliss, A., Bolch, T., Cogley, J.G., Gardner, A., Hagen, J.-O., Hock, R., Huss, M., Kaser, G., Kienholz, C., Pfaffen, W.T., Moholdt, G., Paul, F., Radić, V., Andreassen, L., Bajracharya, S., Barrand, M., Beedle, M., Berthier, E., Bhambr, R., Brown, I., Burgess, E., Burgess, D., Cawkwell, F., Chinn, T., Copland, L., Davies, B., De Angelis, H., Dolgov, E., Earl, L., Filbert, K., Forester, R., Fountain, A., Frey, H., Giffen, B., Glasser, N., Guo, W., Gurney, S., Hagg, W., Hall, D., Haritashya, U.K., Hartmann, G., Helm, C., Herreid, S., Howat, I., Kapustin, G., Khromova, T., König, M., Kohler, J., Kriegel, D., Kutuzov, S., Lavrentiev, I., LeBris, R., Liu, S., Lund, J., Manley, W., Marti, R., Mayer, C., Miles, E., Li, X., Menounos, B., Mercer, A., Mölg, N., Mool, P., Nosenko, G., Negrete, A., Niimura, T., Nuth, C., Pettersson, R., Racoviteanu, A., Ranzi, R., Rastner, P., Rau, F., Raup, B., Rich, J., Rott, H., Sakai, A., Schneider, C., Seliverstov, Y., Sharp, M., Sigurðsson, O., Stokes, C., Way, R., Wheate, R., Winsvold, S., Wolken, G., Wyatt, F., Zhelyagina, N., 2015. Randolph Glacier Inventory – a Dataset of Global Glacier Outlines: Version 5.0. GLIMS Technical Report. . [https://www.glims.org/RGI/00\\_rgi50\\_TechnicalNote.pdf](https://www.glims.org/RGI/00_rgi50_TechnicalNote.pdf)
- Arzhannikov, S.G., Braucher, R., Jolivet, M., Arzhannikova, A.V., Vassallo, R., Chauvet, A., Bourlès, D., Chauvet, F., 2012. History of late Pleistocene glaciations in the central Sayan-Tuva upland (southern Siberia). *Quat. Sci. Rev.* 49, 16–32. <https://doi.org/10.1016/j.quascirev.2012.06.005>.
- Balco, G., 2011. Contributions and unrealized potential contributions of cosmogenic-nuclide exposure dating to glacier chronology, 1990–2010. *Quat. Sci. Rev.* 30, 3–27. <https://doi.org/10.1016/j.quascirev.2010.11.003>.
- Balco, G., 2017. Production rate calculations for cosmic-ray-muon-produced  $^{10}\text{Be}$  and  $^{26}\text{Al}$  benchmarked against geological calibration data. *Quat. Geochronol.* 39, 150–173. <https://doi.org/10.1016/j.quageo.2017.02.001>.
- Balco, G., Briner, J., Finkel, R.C., Rayburn, J.A., Ridge, J.C., Schaefer, J.M., 2009. Regional beryllium-10 production rate calibration for late-glacial northeastern North America. *Quat. Geochronol.* 4, 93–107. <https://doi.org/10.1016/j.quageo.2008.09.001>.
- Balco, G., Stone, J.O., Lifton, N.A., Dunai, T.J., 2008. A complete and easily accessible means of calculating surface exposure ages or erosion rates from  $^{10}\text{Be}$  and  $^{26}\text{Al}$  measurements. *Quat. Geochronol.* 3, 174–195. <https://doi.org/10.1016/j.quageo.2007.12.001>.
- Barr, I.D., Lovell, H., 2014. A review of topographic controls on moraine distribution. *Geomorphology* 226, 44–64. <https://doi.org/10.1016/j.geomorph.2014.07.030>.
- Batbaatar, J., Gillespie, A.R., 2016. Outburst floods of the Maly Yenisei. Part II – new age constraints from Darhad basin. *Int. Geol. Rev.* <https://doi.org/10.1080/00206814.2016.1193452>.
- Batbaatar, J., Gillespie, A.R., Fink, D., Matmon, A., Fujioka, T., 2018. Asynchronous glaciations in arid continental climate. *Quat. Sci. Rev.* 182, 1–19. <https://doi.org/10.1016/j.quascirev.2017.12.001>.
- Benn, D.I., Owen, L.A., 2002. Himalayan glacial sedimentary environments: a framework for reconstructing and dating the former extent of glaciers in high mountains. *Quat. Int.* 97–98, 3–25. [https://doi.org/10.1016/S1040-6182\(02\)00048-4](https://doi.org/10.1016/S1040-6182(02)00048-4).
- Benn, D.I., Hulton, N.R.J., 2010. An Excel™ spreadsheet program for reconstructing the surface profile of former mountain glaciers and ice caps. *Comput. Geosci.* 36, 605–610. <https://doi.org/10.1016/j.cageo.2009.09.016>.
- Blomdin, R., Heyman, J., Stroeve, A.P., Hätteström, C., Harbor, J.M., Gribenski, N., Jansson, K.N., Petrakov, D.A., Ivanov, M.N., Alexander, O., Rudoy, A.N., Walther, M., 2016a. Glacial geomorphology of the Altai and western Sayan mountains, central Asia. *J. Maps* 12, 123–136. <https://doi.org/10.1080/17445647.2014.992177>.
- Blomdin, R., Stroeve, A.P., Harbor, J.M., Lifton, N.A., Heyman, J., Gribenski, N., Petrakov, D.A., Caffee, M.W., Ivanov, M.N., Hätteström, C., Rogozhina, I., Usubaliev, R., 2016b. Evaluating the timing of former glacier culmination in the Tian Shan: a key step towards robust spatial correlations. *Quat. Sci. Rev.* 153, 78–96. <https://doi.org/10.1016/j.quascirev.2016.07.029>.
- Bredstrøup, C.F., Egholm, D.L., Ugelvig, S.V., Pedersen, V.K., 2016. Basal shear stress under alpine glaciers: insights from experiments using the iSOSIA and Elmer/Ice models. *Earth Surf. Dyn.* 4, 159–174. <https://doi.org/10.5194/esurf-4-159-2016>.
- Briner, J.P., Kaufman, D.S., Manley, W.F., Finkel, R.C., Caffee, M.W., 2005. Cosmogenic exposure dating of late Pleistocene moraine stabilization in Alaska. *GSA Bull.* 117, 1108–1120. <https://doi.org/10.1130/B25649.1>.
- Brocklehurst, S.H., Whipple, K.X., 2004. Hypsometry of glaciated landscapes. *Earth Surf. Process. Landforms* 29, 907–926. <https://doi.org/10.1002/esp.1083>.
- Brozovic, N., Burbank, D., Meigs, A., 1997. Climatic limits on landscape development in the northwestern himalaya. *Science* 276, 571–574. <https://doi.org/10.1126/science.276.5312.571>.
- Chen, Y., Li, Y., Wang, Y., Zhang, M., Cui, Z., Yi, C., Liu, G., 2015. Late Quaternary glacial history of the Karlik Range, easternmost Tian Shan, derived from  $^{10}\text{Be}$  surface exposure and optically stimulated luminescence datings. *Quat. Sci. Rev.* 115, 17–27. <https://doi.org/10.1016/j.quascirev.2015.02.010>.
- Cheng, H., Zhang, P.Z., Spötl, C., Edwards, R.L., Cai, Y.J., Zhang, D.Z., Sang, W.C., Tan, M., An, Z.S., 2012. The climatic cyclicity in semiarid-arid central Asia over the past 500,000 years. *Geophys. Res. Lett.* 39, 1–5. <https://doi.org/10.1029/2011GL050202>.
- Chmeleff, J., von Blanckenburg, F., Kossert, K., Jakob, D., 2010. Determination of the  $^{10}\text{Be}$  half-life by multicollector ICP-MS and liquid scintillation counting. *Nucl. Instrum. Methods Phys. Res. Sect. B Beam Interact. Mater. Atoms* 268 (2), 192–199. <https://doi.org/10.1016/j.nimb.2009.09.012>.
- Clark, P.U., Dyke, A.S., Shakun, J.D., Carlson, A.E., Clark, J., Wolfsarth, B., Mitrovica, J.X., Hostettler, S.W., Marshall McCabe, A., 2009. The last glacial maximum. *Science* 325, 710–714. <https://doi.org/10.1126/science.1172873>.
- Cunningham, D., 2005. Active intracontinental transpressional mountain building in the Mongolian Altai: defining a new class of orogen. *Earth Planet. Sci. Lett.* 240, 436–444. <https://doi.org/10.1016/j.epsl.2005.09.013>.
- Dolgushin, L.D., Osipova, G.B., 1989. *Glaciers. Moscow.* 444 pp.
- Eugester, P., Scherer, D., Thiede, R., Codilean, A., Strecker, M., 2016. Rapid last glacial maximum deglaciation in the Indian Himalaya coeval with midlatitude glaciers: new insights from  $^{10}\text{Be}$ -dating of ice-polished bedrock surfaces in the Chandra valley. *NW Himalaya. Geophys. Res. Lett.* 43, 1589–1597. <https://doi.org/10.1002/2013GL058740.Received>.
- Fu, P., Heyman, J., Hätteström, C., Stroeve, A.P., Harbor, J.M., 2012. Glacial geomorphology of the Shalih Shan area, southeastern Tibetan Plateau. *J. Maps* 8, 48–55. <https://doi.org/10.1080/17445647.2012.668762>.
- Ganyushkin, D., Chistyakov, K., Volkov, I., Bantsov, D., Kunaeva, E., Brandová, D., Raab, G., Christl, M., Egli, M., 2018. Palaeoclimate, glacier and treeline reconstruction based on geomorphic evidences in the Mongun-Taiga massif (south-eastern Russian Altai) during the Late Pleistocene and Holocene. *Quat. Int.* 470, 26–37. <https://doi.org/10.1016/j.quaint.2017.12.031>.
- Gibbons, A.B., Megeath, J.D., Pierce, K.L., 1984. Probability of moraine survival in a succession of glacial advances. *Geology* 12, 327–330. [https://doi.org/10.1130/0091-7613\(1984\)12<327:POMSIA>2.0.CO;2](https://doi.org/10.1130/0091-7613(1984)12<327:POMSIA>2.0.CO;2).
- Gillespie, A., Molnar, P., 1995. Asynchronous maximum advances of mountain and continental glaciers. *Rev. Geophys.* 31, 311–364. <https://doi.org/10.1029/95RG00995>.
- Gillespie, A.R., Burke, R.M., Komatsu, G., Bayasgalan, A., 2008. Late Pleistocene glaciers in Darhad basin, northern Mongolia. *Quat. Res.* 69, 169–187. <https://doi.org/10.1016/j.yqres.2008.01.001>.
- Glasser, N.F., Jansson, K.N., 2005. Fast-flowing outlet glaciers of the last glacial maximum Patagonian icefield. *Quat. Res.* 63, 206–211. <https://doi.org/10.1016/j.yqres.2004.11.002>.
- Gosse, J.C., Phillips, F.M., 2001. Terrestrial in situ cosmogenic nuclides: theory and application. *Quat. Sci. Rev.* 20, 1475–1560. [https://doi.org/10.1016/S0277-3791\(00\)00171-2](https://doi.org/10.1016/S0277-3791(00)00171-2).
- Gould, B., 1855. On Peirce's Criterion for the rejection of doubtful observations, with tables for facilitating its application. *Astron. J.* 4, 81–87. <https://doi.org/10.1086/100480>.
- Gribenski, N., Jansson, K., Lukas, S., Stroeve, A., Harbor, J., Blomdin, R., Ivanov, M., Heyman, J., Petrakov, D., Rudoy, A., Clifton, T., Lifton, N., Caffee, M., 2016. Complex patterns of glacier advances during the lateglacial in the Chagan-Uzun valley, Russian Altai. *Quat. Sci. Rev.* 149, 288–305. <https://doi.org/10.1016/j.quascirev.2016.07.032>.
- Gribenski, N., Jansson, K.N., Preusser, F., Harbor, J., Stroeve, A.P., Trauerstein, M., Blomdin, R., Heyman, J., Caffee, M.W., Lifton, N., Zhang, W., 2018. A re-evaluation of MIS 3 glaciation using cosmogenic radionuclide and single grain luminescence ages, Kanas Valley, Chinese Altai. *J. Quat. Sci.* 33, 55–67. <https://doi.org/10.1002/jqs.2998>.
- Grosswald, M.G., Kuhle, M., Fastook, J.L., 1994. Wurm glaciation of lake Issyk-Kul area, Tian Shan mts.: a case study in glacial history of central Asia. *Geojournal* 273–310. <https://doi.org/10.1007/BF00812878>.
- Grosswald, M.G., Rudoy, A.N., 1996. Quaternary glacier-dammed lakes in the mountains of Siberia. *Polar Geogr.* 20, 180–198. <https://doi.org/10.1080/10889379609377599>.
- Hartmann, J., Moosdorf, N., 2012. The new global lithological map database GLiM: a representation of rock properties at the Earth surface. *G-cubed* 13, 1–37. <https://doi.org/10.1029/2012GC004370>.
- Heyman, J., 2014. Paleoglaciation of the Tibetan Plateau and surrounding mountains based on exposure ages and ELA depression estimates. *Quat. Sci. Rev.* 91, 30–41. <https://doi.org/10.1016/j.quascirev.2014.03.018>.
- Heyman, J., Applegate, P.J., Blomdin, R., Gribenski, N., Harbor, J.M., Stroeve, A.P., 2016. Boulder height – exposure age relationships from a global glacial  $^{10}\text{Be}$  compilation. *Quat. Geochronol.* 34, 1–11. <https://doi.org/10.1016/j.quageo.2016.03.002>.
- Heyman, J., Hätteström, C.H., Stroeve, A.P., 2008. Glacial geomorphology of the Bayan har sector of the NE Tibetan plateau. *J. Maps* 4, 42–62. <http://doi.org/10.4113/jom.2008.96>.
- Heyman, J., Stroeve, A.P., Harbor, J.M., Caffee, M.W., 2011. Too young or too old: evaluating cosmogenic exposure dating based on an analysis of compiled boulder exposure ages. *Earth Planet. Sci. Lett.* 302, 71–80. <http://doi.org/10.1016/j.epsl.2010.11.040>.
- Hijmans, R.J., Cameron, S.E., Parra, J.L., Jones, P.G., Jarvis, A., 2005. Very high resolution interpolated climate surfaces for global land areas. *Int. J. Climatol.* 25, 1965–1978. <http://doi.org/10.1002/joc.1276>.
- Horiuchi, K., Matsuzaki, H., Osipov, E., Khlystov, O., Fujii, S., 2004. Cosmogenic  $^{10}\text{Be}$  and  $^{26}\text{Al}$  dating of erratic boulders in the southern coastal area of Lake Baikal, Siberia. *Nucl. Instrum. Methods Phys. Res. Sect. B Beam Interact. Mater. Atoms* 223–224, 633–638. <http://doi.org/10.1016/j.nimb.2004.04.117>.
- Hubert-Ferrari, A., Suppe, J., Van Der Woerd, J., Wang, X., Lu, H., 2005. Irregular earthquake cycle along the southern Tianshan front Aksu area, China. *J. Geophys. Res. B Solid Earth* 110, 1–18. <http://doi.org/10.1029/2003JB002603>.

- Hughes, P.D., Gibbard, P.L., Ehlers, J., 2013. Timing of glaciation during the last glacial cycle: evaluating the concept of a ‘Last Glacial Maximum’ (LGM). *Earth Sci. Rev.* 125, 171–198. <https://doi.org/10.1016/j.earscirev.2013.07.003>.
- Kamp, U., Pan, C.G., 2015. Inventory of glaciers in Mongolia, derived from Landsat imagery from 1989 to 2011. *Geogr. Ann. Ser. A Phys. Geogr.* 97, 653–669. <http://doi.org/10.1111/geoa.12105>.
- Kirkbride, M.P., Winkler, S., 2012. Correlation of Late Quaternary moraines: impact of climate variability, glacier response, and chronological resolution. *Quat. Sci. Rev.* 46, 1–29. <https://doi.org/10.1016/j.quascirev.2012.04.002>.
- Klinge, M., Böhner, J., Lehmkühl, F., 2003. Climate pattern, snow- and Timberlines in the Altai mountains, Central Asia. *Erdkunde* 4, 296–308. <http://www.jstor.org/stable/25647598>.
- Kohl, C.P., Nishizumi, K., 1992. Chemical isolation of quartz for measurements of in-situ-produced cosmogenic nuclides. *Geochim. Cosmochimica Acta* 56, 3583–3587. [https://doi.org/10.1016/0016-7037\(92\)90401-4](https://doi.org/10.1016/0016-7037(92)90401-4).
- Kong, P., Fink, D., Na, C., Huang, F., 2009. Late Quaternary glaciation of the Tianshan, Central Asia, using cosmogenic  $^{10}\text{Be}$  surface exposure dating. *Quat. Res.* 72, 229–233. <https://doi.org/10.1016/j.yqres.2009.06.002>.
- Koppes, M., Gillespie, A.R., Burke, R.M., Thompson, S.C., Stone, J., 2008. Late quaternary glaciation in the Kyrgyz tien Shan. *Quat. Sci. Rev.* 27, 846–866. <https://doi.org/10.1016/j.quascirev.2008.01.009>.
- Korschinek, G., Bergmaier, A., Faestermann, T., Gerstmann, U.C., Knie, K., Rugel, G., Remmert, A., 2010. A new value for the half-life of  $^{10}\text{Be}$  by Heavy-Ion Elastic Recoil Detection and liquid scintillation counting. *Nucl. Instrum. Methods Phys. Res. Sect. B Beam Interact. Mater. Atoms* 268 (2), 187–191. <https://doi.org/10.1016/j.nimb.2009.09.020>.
- Lal, D., 1991. Cosmic ray labeling of erosion surfaces: in situ nuclide production rates and erosion models. *Earth Planet Sci. Lett.* 104, 424–439. [https://doi.org/10.1016/0012-821X\(91\)90220-C](https://doi.org/10.1016/0012-821X(91)90220-C).
- Lehmkuhl, F., 1998. Quaternary glaciations in central and western Mongolia. *Quat. Proc.* 13, 153–167.
- Lehmkuhl, F., 2012. Holocene glaciers in the Mongolian Altai: an example from the Turgen-Kharkhira mountains. *J. Asian Earth Sci.* 52, 12–20. <https://doi.org/10.1016/j.jseas.2011.11.027>.
- Lehmkuhl, F., Klinge, M., Rother, H., Hüller, D., 2016. Distribution and timing of Holocene and late Pleistocene glacier fluctuations in western Mongolia. *Ann. Glaciol.* 57, 1–10. <https://doi.org/10.3189/2016AoG71A030>.
- Lehmkuhl, F., Klinge, M., Stauch, G., 2011. The extent and timing of late Pleistocene glaciations in the Altai and neighbouring mountain systems. In: *Quaternary Glaciations - Extent and Chronology - a Closer Look*, first ed. Elsevier. <https://doi.org/10.1016/B978-0-444-53447-7.00069-6>.
- Lehmkuhl, F., Klinge, M., Stauch, G., 2004. The extent of late Pleistocene glaciations in the Altai and Khangai mountains. In: *Quaternary Glaciations - Extent and Chronology, Part III*, pp. 243–254. [https://doi.org/10.1016/S1571-0866\(04\)80130-80131](https://doi.org/10.1016/S1571-0866(04)80130-80131).
- Lehmkuhl, F., Owen, L.A., 2005. Late Quaternary glaciation of Tibet and the bordering mountains: a review. *Boreas* 34, 87–100. <https://doi.org/10.1080/03009480510012908>.
- Li, H., Ng, F., Li, Z., Qin, D., Cheng, G., 2012. An extended “perfect-plasticity” method for estimating ice thickness along the flow line of mountain glaciers. *J. Geophys. Res. Earth Surf.* 117, 1–11. <https://doi.org/10.1029/2011JF002104>.
- Li, Y., Li, Y., Harbor, J., Liu, G., Yi, C., Caffee, M.W., 2016. Cosmogenic  $^{10}\text{Be}$  constraints on little ice age glacial advances in the eastern tian Shan, China. *Quat. Sci. Rev.* 138, 105–118. <https://doi.org/10.1016/j.quascirev.2016.02.023>.
- Li, Y., Liu, G., Chen, Y., Li, Y., Harbor, J., Stroeve, A.P., Caffee, M., Zhang, M., Li, C., Cui, Z., 2014. Timing and extent of Quaternary glaciations in the Tianger Range, eastern Tian Shan, China, investigated using  $^{10}\text{Be}$  surface exposure dating. *Quat. Sci. Rev.* 98, 7–23. <https://doi.org/10.1016/j.quascirev.2014.05.009>.
- Li, Y., Liu, G., Kong, P., Harbor, J., Chen, Y., Caffee, M., 2011. Cosmogenic nuclide constraints on glacial chronology in the source area of the Urumqi River, Tian Shan, China. *J. Quat. Sci.* 26, 297–304. <https://doi.org/10.1002/jqs.1454>.
- Lifton, N., Beel, C., Hätteström, C., Kassab, C., Rogozhina, I., Heermance, R., Oskin, M., Burbank, D., Blomdin, R., Gribenski, N., Caffee, M., Goehringer, B.M., Heyman, J., Ivanov, M., Li, Y., Li, Y., Petrokov, D., Usubaliyev, R., Codilean, A.T., Chen, Y., Harbor, J., Stroeve, A.P., 2014a. Constraints on the late Quaternary glacial history of the Inylchek and Sary-Dzaz valleys from in situ cosmogenic  $^{10}\text{Be}$  and  $^{26}\text{Al}$ , eastern Kyrgyz Tian Shan. *Quat. Sci. Rev.* 101, 77–90. <https://doi.org/10.1016/j.quascirev.2014.06.032>.
- Lifton, N., Sato, T., Dunai, T.J., 2014b. Scaling in situ cosmogenic nuclide production rates using analytical approximations to atmospheric cosmic-ray fluxes. *Earth Planet Sci. Lett.* 386, 149–160. <https://doi.org/10.1016/j.epsl.2013.10.052>.
- Lindholm, M.S., Heyman, J., 2015. Glacial geomorphology of the Maidika region, Tibetan plateau. *J. Maps* 1–8. <https://doi.org/10.4113/jom.2011.1161>.
- Lisiecki, L.E., Raymo, M.E., 2005. A Pliocene-Pleistocene stack of 57 globally distributed benthic D18O records. *Paleoceanography* 20, 1–17. <https://doi.org/10.1029/2004PA001071>.
- Lowell, T.V., 1995. The application of radiocarbon age estimates to the dating of glacial sequences: An example from the Miami sublobe, Ohio, U.S.A. *Quat. Sci. Rev.* 14, 85–99. [https://doi.org/10.1016/0277-3791\(94\)00113-P](https://doi.org/10.1016/0277-3791(94)00113-P).
- Marrero, S., Phillips, F., Borchers, B., Lifton, N., Aumer, R., Balco, G., 2016. Cosmogenic Nuclide Systematics and the CRONUScalc Program. *Quat. Geochronol.* 31, 160–187. <https://doi.org/10.1016/j.quageo.2015.09.005>.
- Molnar, P., Tappronnier, P., 1975. Cenozoic Tectonics of Asia: Effects of a Continental Collision. *Science* 189, 419–426. <https://doi.org/10.1126/science.189.4201.419>.
- Morén, B., Heyman, J., Stroeve, A.P., 2011. Glacial geomorphology of the central Tibetan Plateau. *J. Maps* 7, 115–125. <https://doi.org/10.4113/jom.2011.1161>.
- Narozhnyi, Y., Zemtsov, V., 2011. Current state of the Altai glaciers (Russia) and trends over the period of instrumental observations 1952–2008. *Ambio* 40, 575–588. <https://doi.org/10.1007/s13280-011-0166-0>.
- Nishizumi, K., Imamura, M., Caffee, M.W., Southon, J.R., Finkel, R.C., McAninch, J., 2007. Absolute calibration of  $^{10}\text{Be}$  AMS standards. *Nucl. Instrum. Meth. Phys. Res. B* 258, 403–413. <https://doi.org/10.1016/j.nimb.2007.01.297>.
- Nishizumi, K., Kohl, C.P., Winterer, E.L., Klein, J., Middleton, R., 1989. Cosmic ray production rates of Be-10 and Al-26 in quartz from glacially polished rocks. *J. Geophys. Res. B* 94, 907–917. <https://doi.org/10.1029/JB094B12p17907>.
- Niimura, T., Sakai, A., Taniguchi, K., Nagai, H., Lamsal, D., Tsutaki, S., Kozawa, A., Hoshina, Y., Tekenaka, S., Omiya, S., Tsunematsu, K., Tshering, P., Fujita, K., 2015. The GAMDAM Glacier Inventory: a quality controlled inventory of Asian glaciers. *Cryosphere* 9, 849–864. <https://doi.org/10.5194/tcd-8-2799-2014>.
- Oerlemans, J., Anderson, B., Hubbard, A., Huylebroeck, P., Jóhannesson, T., Knap, W.H., Schmeits, M., Stroeve, A.P., van de Wal, R.S.W., Wallinga, J., Zuo, Z., 1998. Modelling the response of glaciers to climate warming. *Clim. Dynam.* 14, 267–274. <https://doi.org/10.1007/s003820050222>.
- Peirce, B., 1852. Criterion for the rejection of doubtful observations. *Astron. J.* 2, 161–163. <https://doi.org/10.1086/100259>.
- Peirce, B., 1877. On Peirce’s Criterion. *Proc. Am. Acad. Arts Sci.* 13, 348–351. <https://doi.org/http://dx.doi.org/10.2307/251138498>.
- Phillips, F.M., Argento, D.C., Balco, G., Caffee, M.W., Clem, J., Dunai, T.J., Finkel, R., Goehringer, B., Gosse, J.C., Hudson, A.M., Jull, A.J.T., Kelly, M.A., Kurz, M., Lal, D., Lifton, N., Marrero, S.M., Nishizumi, K., Reedy, R.C., Schaefer, J., Stone, J.O.H., Swanson, T., Zreda, M.G., 2016. The CRONUS-Earth Project: A synthesis. *Quat. Geochronol.* 31, 119–154. <https://doi.org/10.1016/j.quageo.2015.09.006>.
- Putkonen, J., Swanson, T., 2003. Accuracy of cosmogenic ages for moraines. *Quat. Res.* 59, 255–261. [https://doi.org/10.1016/S0033-5893\(03\)00006-1](https://doi.org/10.1016/S0033-5893(03)00006-1).
- Reuther, A., 2007. PhD thesis. Relief Boden Palaeoklima Band. Surface Exposure Dating of Glacial Deposits from the Last Glacial Cycle – Evidence from the Eastern Alps, the Bavarian Forest, the Southern Carpathians and the Altai Mountains, vol. 21. pp. 213 ISBN: 9783443090210.
- Reuther, A.U., Herget, J., Ivy-Ochs, S., Borodavko, P., Kubik, P.W., Heine, K., 2006. Constraining the timing of the most recent cataclysmic flood event from ice-dammed lakes in the Russian Altai Mountains, Siberia, using cosmogenic in situ  $^{10}\text{Be}$ . *Geology* 34, 913–916. <https://doi.org/10.1130/G22755A.1>.
- Ross, S.M., 2003. Peirce’s criterion for the elimination of suspect experimental data. *J. Eng. Technol.* 20, 1–12. <http://classes.engineering.wustl.edu/che473/handouts/OutlierRejection.pdf>.
- Rother, H., Lehmkuhl, F., Fink, D., Nottebaum, V., 2014. Surface exposure dating reveals MIS-3 glacial maximum in the Khangai Mountains of Mongolia. *Quat. Res.* 82, 297–308. <https://doi.org/10.1016/j.yqres.2014.04.006>.
- Rudoy, A.N., 2002. Glacier-dammed lakes and geological work of glacial super floods in the Late Pleistocene, Southern Siberia, Altai Mountains. *Quat. Int.* 87, 119–140. [https://doi.org/10.1016/S1040-6182\(01\)00066](https://doi.org/10.1016/S1040-6182(01)00066).
- Rudoy, A.N., Baker, V.R., 1993. Sedimentary effects of cataclysmic late Pleistocene glacial outburst flooding, Altay Mountains, Siberia. *Sediment. Geol.* 85 (1–4), 53–62. [https://doi.org/10.1016/0037-0738\(93\)90075-G](https://doi.org/10.1016/0037-0738(93)90075-G).
- Rupper, S., Roe, G., 2008. Glacier Changes and Regional Climate: A Mass and Energy Balance Approach. *J. Clim.* 21, 5384–5401. <https://doi.org/10.1175/2008JCLI2219.1>.
- Rupper, S., Roe, G., 2009. Spatial patterns of Holocene glacier advance and retreat in Central Asia. *Quat. Res.* 72, 337–346. <https://doi.org/10.1016/j.yqres.2009.03.007>.
- Scherler, D., Bookhagen, B., Strecker, M.R., 2011. Hillslope-glacier coupling: The interplay of topography and glacial dynamics in High Asia. *J. of Geophys. Res.* 116, 1–21. <https://doi.org/10.1029/2010JF001751>.
- Sergienko, O., Hindmarsh, R.C., 2013. Regular Patterns in Frictional Resistance of Ice-Stream Beds Seen by Surface Data Inversion. *Science* 342, 1086–1089. <https://doi.org/10.1126/science.1243903>.
- Shakun, J.D., Clark, P., He, F., Lifton, N.A., Liu, Z., Otto-Bliesner, B.L., 2015. Regional and global forcing of glacier retreat during the last deglaciation. *Nat. Commun.* 6, 8059. <https://doi.org/10.1038/ncomms9059>.
- Sharma, P., Bourgeois, M., Elmore, D., Granger, D., Lipschutz, M.E., Ma, X., Miller, T., Mueller, K., Rickey, F., Simms, P., Vogt, S., 2000. PRIME lab AMS performance, upgrades and research applications. *Nucl. Instruments Methods Phys. Res. Sect. B-Beam Interact. with Mater. Atoms* 172, 112–123. [https://doi.org/10.1016/S0168-583X\(00\)00132-4](https://doi.org/10.1016/S0168-583X(00)00132-4).
- Smith, S.G., Wegmann, K.W., Ancuta, L.D., Gosse, J.C., Hopkins, C.E., 2016. Paleotopography and erosion rates in the central Hangay Dome, Mongolia: Landscape evolution since the mid-Miocene. *J. Asian Earth Sci.* 125, 37–57. <https://doi.org/10.1016/j.jseas.2016.05.013>.
- Stone, J.O., 2000. Air pressure and cosmogenic isotope production. *J. Geophys. Res.* 105, 753–759. <https://doi.org/10.1029/2000JB900181>.
- Stroeve, A.P., Hätteström, C., Heyman, J., Kleman, J., Morén, B.M., 2013. Glacial geomorphology of the Tian Shan. *J. Maps* 9, 505–512. <https://doi.org/10.1080/17445647.2013.820879>.
- Telbisz, T., Kovács, G., Székely, B., Szabó, J., 2013. Topographic swath profile analysis: a generalization and sensitivity evaluation of a digital terrain analysis tool. *Z. Geomorphol.* 57, 485–513. <https://doi.org/10.1127/0372-8854/2013/0110>.
- Thompson, L.G., Yao, T., Davis, M., Henderson, K., Mosley-Thompson, E., Lin, P.-N., Beer, J., Synal, H.-A., Cole-Dai, J., Bolzan, J., 1997. Tropical Climate Instability: The Last Glacial Cycle from a Qinghai-Tibetan Ice Core. *Science* 276, 1821–1825. <https://doi.org/10.1126/science.276.5320.1821>.
- Tronov, M.V., 1949. Essays about Altai Glaciation. *Geographgiz, Moscow*.
- Uppala, S.M., Kållberg, P.W., Simmons, A.J., Andrae, U., Bechtold, V.D.C., Fiorino, M.,

- Gibson, J.K., Haseler, J., Hernandez, A., Kelly, G.A., Li, X., Onogi, K., Saarinen, S., Sokka, N., Allan, R.P., Andersson, E., Arpe, K., Balmaseda, M.A., Beljaars, A.C.M., Berg, L., Van De Bidlot, J., Bormann, N., Caires, S., Chevallier, F., Dethof, A., Dragosavac, M., Fisher, M., Fuentes, M., Hagemann, S., Hölm, E., Hoskins, B.J., Isaksen, L., Janssen, P.A.E.M., Jenne, R., McNally, A.P., Mahfouf, J.-F., Morcrette, J.-J., Rayner, N.A., Saunders, R.W., Simon, P., Sterl, A., Trenberth, K.E., Untch, A., Vasiljevic, D., Viterbo, P., Woollen, J., 2005. The ERA-40 re-analysis. *Q. J. R. Meteorol. Soc.* 131, 2961–3012. <http://doi.org/10.1256/qj.04.176>.
- Winkler, M.G., Wang, P.K., 1993. The late Quaternary vegetation and climate of China. In: Wright, H.E., Kutzbach, J.E., Webb, T., Rudiman, W.F., StreetPerrott, F.A., Bartlein, P.J. (Eds.), *Global Climates since the Last Glacial Maximum*. University of Minnesota Press, Minneapolis, pp. 221–261.
- Wünnemann, B., Hartmann, K., Janssen, M., Zhang, H.C., 2007. Responses of Chinese desert lakes to climate instability during the past 45,000 years. *Dev. Quat. Sci.* 9, 11–24. [https://doi.org/10.1016/S1571-0866\(07\)09003-3](https://doi.org/10.1016/S1571-0866(07)09003-3).
- Yin, A., 2010. Cenozoic tectonic evolution of Asia: A preliminary synthesis. *Tectonophysics* 488, 293–325. <https://doi.org/10.1016/j.tecto.2009.06.002>.
- Zech, R., 2012. A late Pleistocene glacial chronology from the Kitschi-Kurumdu Valley, Tien Shan (Kyrgyzstan), based on  $^{10}\text{Be}$  surface exposure dating. *Quat. Res.* 77, 281–288. <https://doi.org/10.1016/j.yqres.2011.11.008>.
- Zech, R., Glaser, B., Sosin, P., Kubik, P.W., Zech, W., 2005. Evidence for long-lasting landform surface instability on hummocky moraines in the Pamir Mountains (Tajikistan) from  $^{10}\text{Be}$  surface exposure dating. *Earth Planet Sci. Lett.* 237, 453–461. <https://doi.org/10.1016/j.epsl.2005.06.031>.
- Zhang, M., Chen, Y., Li, Y., Liu, G., 2016. Late Quaternary glacial history of the Nalati Range, central Tian Shan, China, investigated using  $^{10}\text{Be}$  surface exposure dating. *J. Quat. Sci.* 31, 659–670. <https://doi.org/10.1002/jqs.2891>.
- Zhao, J.D., Yin, X.F., Harbor, J.M., Lai, Z.P., Liu, S.Y., Li, Z.Q., 2013. Quaternary glacial chronology of the Kanas River valley, Altai Mountains, China. *Quat. Int.* 311, 44–53. <https://doi.org/10.1016/j.quaint.2013.07.047>.